RESEARCH ARTICLE

Extended Micromechanical Model for the Hyperelastic Behavior of Elastomers and Identification of Material Parameters Using the Particle Swarm Optimization (PSO) Algorithm

Ayoub Ouardi[1,*], **Adnane Boukamel**[2] **and Noureddine Damil**[1]

[1] Centrale Casablanca, Centre de Recherche Systèmes Complexes et Interactions, Ville Verte, Bouskoura 27182, Morocco
[2] Ecole Centrale de Pekin, Beihang University, Beijing 100191, China

Abstract

In this work, we propose a new four-parameter micromechanical model to describe the hyperelastic behavior of elastomeric materials. The proposed model extends and improves a previously developed three-parameter micromechanical approach. As in earlier studies, the constitutive behavior is obtained by minimizing the potential energy of a Representative Volume Element (RVE) composed of multiple macromolecular chains. Each chain segment is modeled as a linear spring with stiffness K, acting in both tension and compression. To account for rotational flexibility between consecutive segments, nonlinear torsional springs are introduced, whose behavior is described as the sum of two contributions: a sigmoidal function characterized by a limiting moment M_0 and a parameter a, and a linear term with stiffness b representing resistance during segment unfolding. This four-parameter formulation (a, b, M_0, and K) provides greater flexibility for parameter identification and improves the accuracy of the predicted mechanical response. Two identification strategies are considered: a physically motivated approach and an optimization-based method using the Particle Swarm Optimization (PSO) algorithm, which minimizes the discrepancy between numerical predictions and experimental data without requiring gradient information, making it particularly suitable for implicit numerical models. Numerical simulations are carried out on a two-dimensional RVE composed of four chains, and results are compared with Treloar's (1943) experimental data and selected statistical models under uniaxial tension, pure shear, and equibiaxial tension.

Keywords: micromechanical model, macro-molecular polymer chains, rubber-like materials, parameter identification, Particle Swarm Optimization (PSO), hyperelastic, Asymptotic Numerical Method (ANM).

Submitted: 28 March 2026
Accepted: 27 May 2026
Published: 08 June 2026

Vol. 1, **No.** 1, 2026.
10.62762/JCN.2026.518617

***Corresponding author:**
✉ Ayoub Ouardi
ayoub.ouardi@centrale-casablanca.ma

Citation
Ouardi, A., Boukamel, A., & Damil, N. (2026). Extended Micromechanical Model for the Hyperelastic Behavior of Elastomers and Identification of Material Parameters Using the Particle Swarm Optimization (PSO) Algorithm. *Journal of Carbon Neutrality*, 1(1), 38–63.

© 2026 by the Authors. Published by Institute of Central Computation and Knowledge. This is an open access article under the CC BY license (https://creativecommons.org/licenses/by/4.0/).

1 Introduction

Elastomers exhibit mechanical behavior that differs significantly from that of conventional engineering materials, due to their ability to undergo extremely large deformations while remaining essentially reversible. This remarkable response originates from their polymer network structure, which governs their behavior across multiple length scales. In many engineering applications, elastomeric components are subjected to complex multiaxial loading conditions, making the development of reliable predictive tools essential. Such tools require constitutive models capable of capturing strong nonlinearities, strain-stiffening effects at large deformations, and the microstructural evolution occurring under finite deformation. Moreover, in the context of global carbon neutrality objectives, the reliability and durability of elastomeric components have become increasingly critical in emerging clean-energy technologies such as electric vehicles, wind turbines, and hydrogen systems. Improving the predictive capability of hyperelastic models can therefore contribute to the design of more durable and sustainable elastomer-based components, thereby enhancing energy efficiency and reducing life-cycle emissions.

At the microscopic scale, elastomers consist of a three-dimensional network of long polymer chains linked by chemical cross-links and constrained by physical entanglements. In their initial configuration, these chains adopt a random coil conformation corresponding to a state of maximum entropy. The application of mechanical loading disrupts this equilibrium by inducing progressive chain alignment and unfolding along the principal directions of deformation, resulting in a highly nonlinear macroscopic response. The finite extensibility of polymer chains, together with topological constraints induced by entanglements, plays a key role in the gradual stiffening of the material and in limiting its ultimate elongation. At sufficiently large deformations, additional mechanisms may arise, such as deformation-induced crystallization in certain elastomers [4–6]. This phenomenon modifies the effective network structure by introducing new physical bonds, leading to a marked increase in stiffness. The interaction between entropic elasticity, network constraints, and microstructural transformations results in a complex overall behavior that is difficult to capture using purely phenomenological approaches.

To better describe the mechanical response of polymer networks at the microscopic scale, numerous constitutive models have been developed, based either on phenomenological formulations or on statistical polymer mechanics. These models aim to represent key mechanisms such as chain unfolding, limited extensibility, and topological constraints arising from cross-links and entanglements. Among models derived from statistical polymer mechanics, the eight-chain model proposed by Arruda and Boyce [7] is a widely recognized reference. Based on an idealized representation of the polymer network and a non-Gaussian description of chain behavior accounting for finite extensibility, this model successfully reproduces the characteristic strain-stiffening behavior of elastomers at large deformations. Its relatively simple structure and clear microstructural interpretation explain its widespread use. Comparative studies, notably the work of [8], have confirmed the relevance of this approach by comparing several models against the classical Treloar experiments under various loading conditions. This study highlighted the ability of microstructurally motivated formulations to consistently reproduce the nonlinear response of rubbers over a wide range of deformations. The Worm-Like Chain (WLC) model [8–11] is widely used to describe the behavior of semi-flexible polymer chains and the associated strain stiffening at large deformations.

At the same time, phenomenological models have been developed to provide compact and easily identifiable formulations. For instance, the reformulation of Gent's model proposed by Pucci and Saccomandi [12] retains the concept of finite extensibility while reducing the number of parameters, offering a compromise between accuracy and simplicity.

For soft biological tissues, various constitutive models have also been proposed to capture their highly nonlinear behavior [13, 14].

More recently, multiscale approaches have been introduced to explicitly link microstructure and macroscopic response, for example by coupling non-Gaussian statistical models with finite element formulations [15], or by combining cross-linked and entangled network descriptions with physically meaningful parameters [16].

In previous works [1] and [2], a three-parameter micromechanical model was developed in both two- and three-dimensional settings to describe the hyperelastic behavior of elastomers. This approach successfully reproduces the three main phases

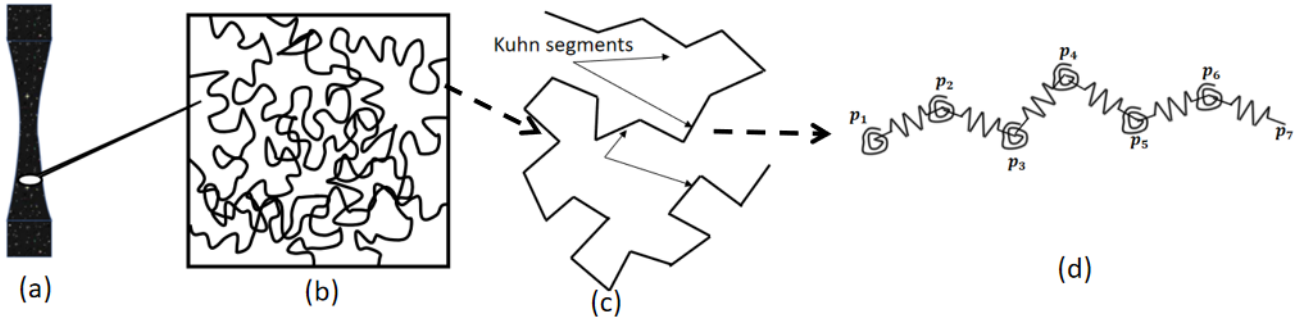

Figure 1. (a): An elastomer material. (b): A Representative Volume Element (RVE) constituted by M chains C_k. (c) A single macromolecular chain formed of n_k Kuhn segments. (d) A single chain represented by n_k elastic springs and n_k spiral springs.

observed in elastomer behavior: (i) disentanglement of macromolecular chains, (ii) progressive unfolding of chain segments, and (iii) strain-stiffening at large deformations. Numerical simulations performed on various RVEs and comparisons with experimental data demonstrated the robustness and predictive capability of this model.

In the present study, we propose an extended and improved version of this approach. Each macromolecular chain is modeled as a sequence of linear springs connected by nonlinear torsional springs. Unlike the previous three-parameter formulation, the nonlinear behavior of the torsional springs is expressed as the sum of two contributions: a sigmoidal function characterized by a threshold M_0 and a parameter a, describing the activation of rotational mechanisms during chain disentanglement, and a linear term with stiffness b, representing resistance during segment unfolding. This formulation leads to a four-parameter micromechanical model that offers greater flexibility and improved accuracy. The nonlinear equilibrium equations are obtained by minimizing the potential energy of the RVE and are solved numerically using the Asymptotic Numerical Method (ANM).

The Asymptotic Numerical Method (ANM) is a numerical technique dedicated to the solution of nonlinear problems. It is based on a Taylor series expansion to compute the solution branch by branch [17], in contrast to the point-by-point Newton–Raphson algorithm. ANM has been successfully applied in structural mechanics, fluid mechanics, and in the analysis of buckling and bifurcation phenomena [18–26].

To evaluate the performance of the model, we consider a four-chain RVE and compare numerical predictions with Treloar's (1943) experimental data under three loading conditions: uniaxial tension, pure shear, and equibiaxial tension. Two identification strategies are investigated: a physically motivated approach and an optimization-based approach using the Particle Swarm Optimization (PSO) algorithm [27–30]. The latter minimizes the discrepancy between the numerical response and the experimental data without requiring an explicit stress–strain relationship, making it particularly suitable for the proposed model.

The paper is organized as follows. In Section 2, we present the three-parameter model together with several numerical simulations, discussing the influence of the material parameters and the accuracy of the model through comparisons with the experimental results of Treloar (1944). In Section 3, we develop the extended four-parameter model and present numerical simulations illustrating the influence of the model parameters, along with comparisons against the experimental results, the three-parameter model, and several classical statistical models. The results show that the extended model provides greater flexibility in parameter fitting and is therefore more accurate in predicting the experimental data than the three-parameter model.

2 Presentation of the micromechanical model for the hyperelastic behavior of elastomers

2.1 Description of the micromechanical model

In elastomeric materials (Figure 1(a)), we consider a two-dimensional Representative Volume Element (RVE) composed of M randomly distributed macromolecular chains C_k (Figure 1(b)), each consisting of n_k Kuhn segments (Figure 1(c)) [31]. Following our previous work ([1] and [2]), each macromolecular chain is modeled using micromechanical elements. Each chain is represented as a sequence of n_k linear elastic springs connected by n_k nonlinear torsional springs (Figure 1(d)).

The tensile strain energy of segment i in chain k is defined as:

$$w_{t_i}^k\left(\Delta l_i^k\right) = \frac{1}{2}K\left(\Delta l_i^k\right)^2 \tag{1}$$

where the elongation Δl_i^k of each segment i is given by $\Delta l_i^k = l_i^k - L_i^k$ and L_i^k denote the initial lengths.

The rotational flexibility between two consecutive segments is modeled through a nonlinear bending energy expressed as:

$$w_{b_i}^k\left(\Delta {\varphi_i}^k\right) = a \cdot M_0 \cdot \ln\left(\cosh\left(\frac{\Delta\varphi_i^k}{a}\right)\right) \tag{2}$$

where the variation $\Delta\varphi_i^k$ of the angles between two consecutive segments is given by $\Delta\varphi_i^k = (\varphi_i^k - \varphi_{i-1}^k) - (\Phi_i^k - \Phi_{i-1}^k)$ and Φ_i^k represents the initial angles of the segments. The proposed model is characterized by 3 material parameters K, a, M_0 which represent respectively the stiffness of the segments, the bending angle and an asymptotic moment of the model. The behavior of each elastic spiral is given by the nonlinear relationship between the moment M_i^k and the variation of the angles $\Delta\varphi_i^k$ between each consecutive pair of segments. The moment–rotation relationship for the torsional springs is obtained by differentiation of the bending energy (2):

$$M_i^k\left(\Delta {\varphi_i}^k\right) = M_0 \cdot \tanh\left(\frac{\Delta\varphi_i^k}{a}\right) \tag{3}$$

This formulation describes a progressive increase in bending moment with angular deformation, starting from an initial stiffness M_0/a and asymptotically approaching the limit value M_0, corresponding to full chain unfolding (see Figure 2) [32].

The total strain energy $W(l_i^k, \varphi_i^k)$ of the RVE, is obtained by summing the contributions of all chains C_k. The potential energy of the system can then be written in the following form:

$$E_p\left(l_i^k, \varphi_i^k\right) = \sum_{k=1}^{M}\left(\sum_{i=1}^{n_k} w_{t_i}^k\left(\Delta l_i^k\right) + w_{b_i}^k\left(\Delta\varphi_i^k\right)\right) \tag{4}$$

As boundary conditions, a macroscopic deformation gradient $\mathbb{F}$ is applied on the boundary ∂V, leading to the displacement field:

$$\boldsymbol{u} \;=\; \boldsymbol{u}^d \;=(\mathbb{F}-\mathbb{I})\boldsymbol{X} \quad \text{on } \partial V \tag{5}$$

where $\boldsymbol{X}$ denotes the coordinates of the points located on the boundary ∂V of the RVE in the reference configuration.

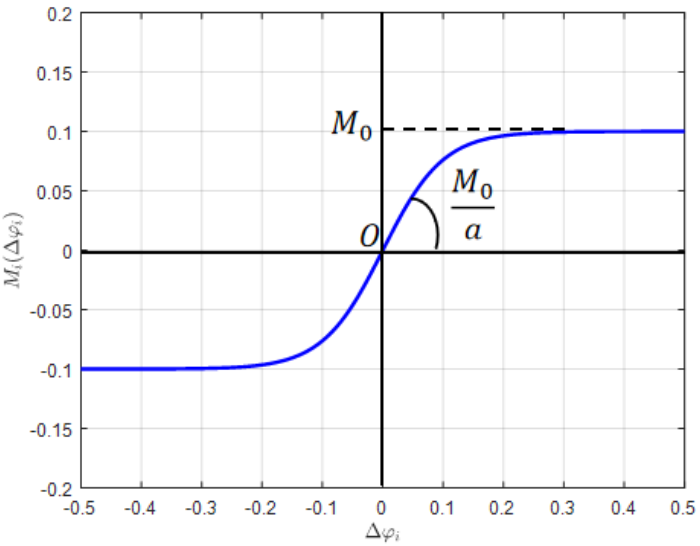

Figure 2. Nonlinear behavior of the spiral springs: the moment M_i as a function of the variation of the angles $\Delta\varphi_i$, for $a = 0.1$ and $M_0 = 0.1$.

If junctions between chains are included, additional kinematic constraints must be introduced. For R junctions, compatibility conditions are written as:

$$\begin{cases} u_r^{k_1,p_1} - u_r^{k_2,p_2} = g_r^u = 0 \\ v_r^{k_1,p_1} - v_r^{k_2,p_2} = g_r^v = 0 \end{cases} \qquad r = 1,\ldots,R \tag{6}$$

The equilibrium configuration is obtained by minimizing the potential energy (4) under constraints (5) and (6). This leads to the following Lagrangian:

$$\begin{aligned} \mathcal{L}\left(l_i^k, \varphi_i^k, \eta_x^k, \eta_y^k, \xi_r^u, \xi_r^v, \mathbb{F}\right) &= E_p\left(l_i^k, \varphi_i^k\right) \\ &- \sum_{k=1}^{M}\sum_{j=1}^{n_k}(\eta_x^{j,k}(u_j^k - u_j^{d,k}) + \eta_y^{j,k}(v_j^k - v_j^{d,k})) \\ &- \sum_{r=1}^{R}(\xi_r^u g_r^u + \xi_r^v g_r^v) \end{aligned} \tag{7}$$

where $k = 1,\ldots,M$; $j = 1,\ldots,n_k$ and $\eta_x^{j,k}$, $\eta_y^{j,k}$, ξ_r^u, ξ_r^v, for $r = 1,\ldots,R$, are the Lagrange multipliers.

The components of the displacements u_j^k and v_j^k in (7) can be expressed in terms of the variables l_p^k and φ_p^k:

$$\begin{aligned} u_j^k &= \textstyle\sum_{p=0}^{j-1}\left(l_p^k\cos\varphi_p^k - L_p^k\cos\Phi_p^k\right) \\ v_j^k &= \textstyle\sum_{p=0}^{j-1}\left(l_p^k\sin\varphi_p^k - L_p^k\sin\Phi_p^k\right) \end{aligned} \tag{8}$$

Hence, the nonlinear equilibrium equations are obtained from the stationarity condition:

$$\delta\mathcal{L} = 0 \tag{9}$$

depend on the variables $l_j^k, \varphi_j^k, \eta_x^{j,k}, \eta_y^{j,k}, \xi_r^u, \xi_r^v$, and on the imposed gradient $\mathbb{F}$.

By numerically solving the equilibrium problem (9), the constitutive law relating the imposed macroscopic deformation tensor $\mathbb{F}$ to the macroscopic stresses applied to the RVE can be established. The macroscopic first Piola–Kirchhoff stress tensor $\bar{\Pi}_{ij}$ is given by [1, 33]:

$$\bar{\Pi}_{ij} = \frac{1}{V}\int_{\partial V} \Pi_{ik} x_j n_k dl = \frac{1}{V}\sum_{p\in\partial V} \eta_i^p x_j^p \tag{10}$$

where Π_{ik} is the microscopic first Piola–Kirchhoff stress tensor. The components of the forces are given by $(\Pi_{ik} n_k dl)^p = \eta_i^p$.

2.2 Resolution algorithm

The nonlinear equilibrium equations (9) can be written in the following form:

$$\{R(\{V\},\lambda)\} = \{0\} \tag{11}$$

where λ is a control parameter governing the evolution of the prescribed macroscopic deformation tensor $\mathbb{F}$ (for example, in uniaxial tension, λ corresponds to the component $\mathbb{F}_{11}$) and $\{V\}$ denotes the global mixed unknown vector containing all the unknowns of the problem.

In this work we propose to solve the nor problem (11) using the Asymptotic Num Method (ANM). In the ANM algorithm [17 solution $(\{V\},\lambda)$ of the nonlinear problem (determined branch by branch, and each brar represented by truncated Taylor series at order with respect to a path parameter β:

$$\begin{cases} \{V\}(\beta) = \{V\}_0 + \sum_{q=1}^{N_{order}} \beta^q \{V\}_q \\ \lambda(\beta) = \lambda_0 + \sum_{q=1}^{N_{order}} \beta^q \lambda_q \end{cases} \quad \text{where } \beta \in [($$

where $(\{V\}_0, \lambda_0)$ is an initial given solution problem (11). By identifying the terms of the series, with the same power of β, we obtain a rec sequence of linear problems satisfied by the of order q of the Taylor series (12) $\{V\}_q$. Th parameter β is defined from an auxiliary condition:

$$\beta = \langle \{V\} - \{V\}_0 \rangle \{V\}_1 + (\lambda - \lambda_0)\lambda_1 \tag{13}$$

and β must be lower than a maximal value that has been estimated in [17]:

$$\beta_{max}^j = \left(\varepsilon \frac{||\{V\}_1||}{||\{V\}_{N_{order}}||} \right)^{\frac{1}{N_{order}-1}} \tag{14}$$

where ε is a tolerance parameter. Once the branch^j and β_{max}^j are calculated, we look for the branch^{j+1} by continuation, taking as the new starting point the point defined by $\{V\}_0 = \{V\}(\beta_{max}^j)$ and $\lambda_0 = \lambda(\beta_{max}^j)$.

For all the simulations reported in this paper, the parameters N_{order} and ε were fixed at $N_{order} = 20$ and $\varepsilon = 10^{-8}$, respectively.

2.3 Numerical results and Discussion

2.3.1 *Influence of the three parameters of the model a, M_0 and K*

In this section, we analyze the influence of three material parameters a, M_0, and K on the constitutive response of the model. We consider a four-chain RVE, where each chain contains 65 segments of length $L_i = 5nm$, resulting in a total of 260 segments. The four chains connect the four vertices of the RVE to its center through a junction point (see Figure 3). Three parametric studies are performed:

- Variation of a (with M_0 and K fixed)
- Variation of M_0 (with a and K fixed)
- Variation of K (with a and M_0 fixed)

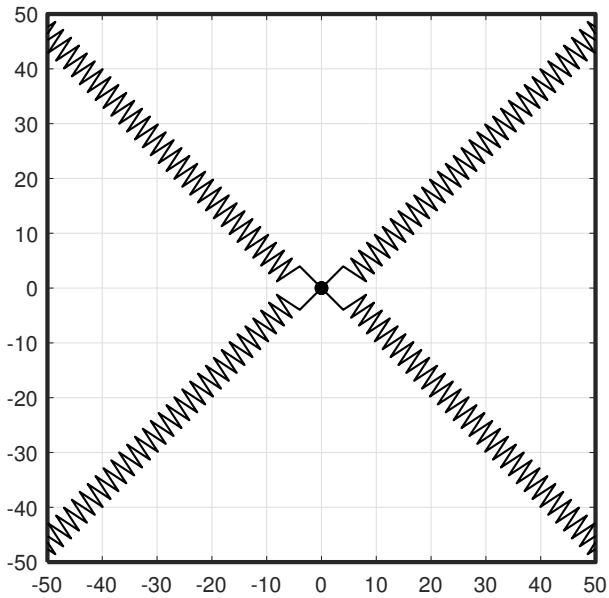

Figure 3. Four-chain RVE

The loading considered corresponds to uniaxial tension, associated with the following deformation gradient tensor: $\mathbb{F} = \begin{bmatrix} \lambda & 0 & 0 \\ 0 & \lambda^{-1/2} & 0 \\ 0 & 0 & \lambda^{-1/2} \end{bmatrix}$. For thin specimens, a two-dimensional modeling approach is

adopted under the plane stress assumption, leading to the following expression of the deformation gradient tensor: $\mathbb{F} = \begin{bmatrix} \lambda & 0 \\ 0 & \lambda^{-1/2} \end{bmatrix}$.

The results in Figure 4 show that:

- The parameter a controls the slope of the initial (disentanglement) phase (see Figure 4(a)).
- The parameter M_0 governs the amplitude of the intermediate (chain unfolding) phase (see Figure 4(b)).
- The parameter K determines the stiffness in the large-deformation regime (see Figure 4(c)).

2.3.2 *Microstructural influence*

From the previous discussion, it can be concluded that each parameter has a clear and physically meaningful influence on a specific phase of the mechanical response. However, none of these parameters affects the strain range preceding the strain-stiffening regime at large deformations, which is an important characteristic of the hyperelastic behavior of elastomers.

Furthermore [34], the experimental results show that the deformation required to reach the stiffening phase under large deformation depends on the nature and microstructure of the elastomer (number of segments in the macromolecular chains, distribution of macromolecular chains, crosslink density, etc.). Based on the experiments, elastomers are classified into four types according to their stiffening deformation: low extensibility elastomers with a stiffening deformation between 40% and 80%; moderate extensibility elastomers with a stiffening deformation between 80% and 180%; high extensibility elastomers with a stiffening deformation between 180% and 300%; and extreme extensibility elastomers with a stiffening deformation greater than 300%.

So we conducted an additional study to investigate the influence of the number of segments per chain while keeping the same RVE geometry. The number of segments is therefore varied systematically (see Figure 5(a,b,c,d)).

The results show that increasing the number of segments delays the onset of strain stiffening. This behavior reflects a more progressive unfolding of the chains and extends the deformation range associated with the first two phases of the mechanical response. In Figure 6(a), we observe that the first RVE of 124 segments starts its stiffening phase at a deformation $\lambda = 3$, the second RVE of 172 segments starts its stiffening phase at a deformation $\lambda = 4.5$, the third RVE of 204 segments starts its stiffening phase at a deformation $\lambda = 5.2$, and the fourth RVE of 260 segments starts its stiffening phase at a deformation $\lambda = 6.5$.

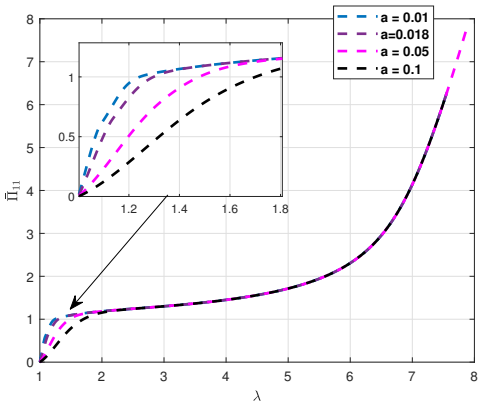

(a) Influence of parameters a for $M_0 = 1.5\ 10^{-4}\ N.nm$ and $K = 3.5\ 10^{-4}\ N/nm$

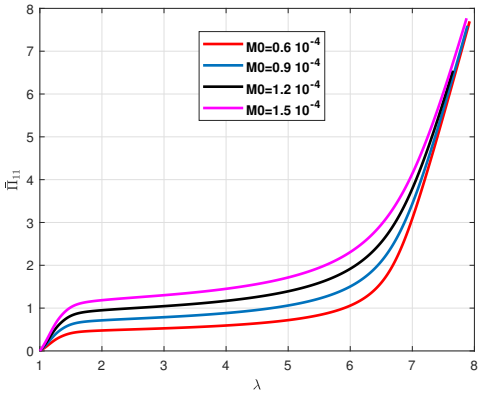

(b) Influence of parameters M_0 for $a = 0.05\ rad$ and $K = 3.5\ 10^{-4}\ N/nm$

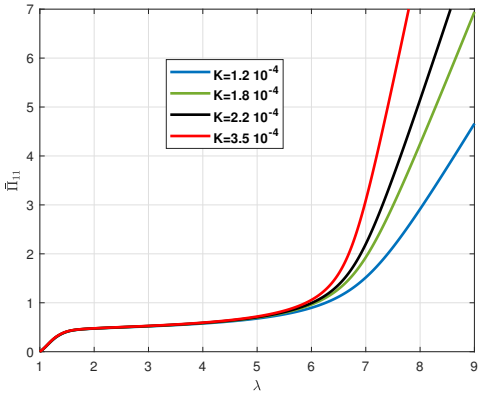

(c) Influence of parameters K for $a = 0.05\ rad$ and $M0 = 0.6\ 10^{-4}\ N.nm$

Figure 4. Influence of the three material parameters a, M_0, and K of the proposed micromechanical model.

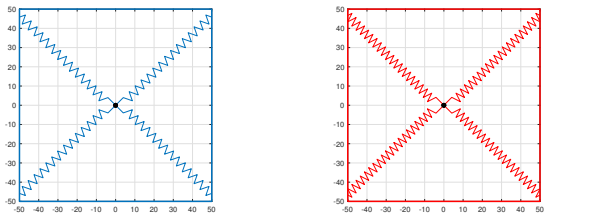

(a) RVE formed by 124 segments, 31 segments per chain

(b) RVE formed by 172 segments, 43 segments per chain

(c) RVE formed by 204 segments, 51 segments per chain

(d) RVE formed by 260 segments, 65 segments per chain

Figure 5. The four RVEs used to study the influence of the number of segments per RVE.

These observations lead us to conclude that increasing the number of segments in macromolecular chains while maintaining the same end-to-end distances gives macromolecular chains more time to unfold, thus increasing the range of the first and second phases before reaching stiffening under large deformation. In Figure 6(b), we also present stress $\bar{\Pi}_{11}$ as a function of strain λ divided by the number of segments N. We note that, regardless of the number of segments used to model macromolecular chains, the response established by the proposed micromechanical approach always converges to a unique behavior.

We note that all the parameters investigated exhibit a specific and physically meaningful influence on the constitutive behavior described by the proposed micromechanical approach, unlike several phenomenological and statistical models reported in the literature. This advantage allows, on the one hand, the use of physically motivated parameter identification based on experimental data and, on the other hand, facilitates convergence when employing optimization algorithms that minimize the discrepancy between the experimental data and the numerical response.

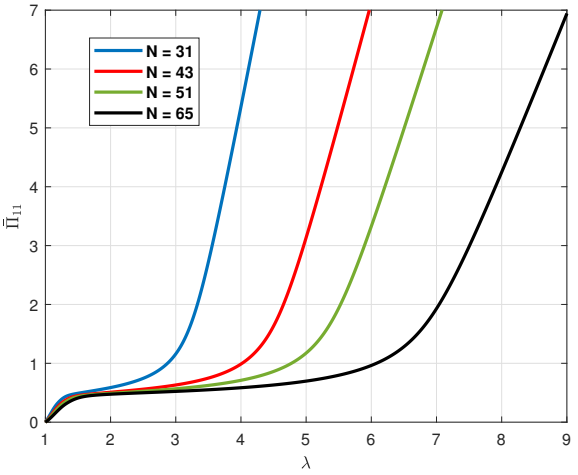

(a) Behavior law: $\bar{\Pi}_{11}$ as a function of λ

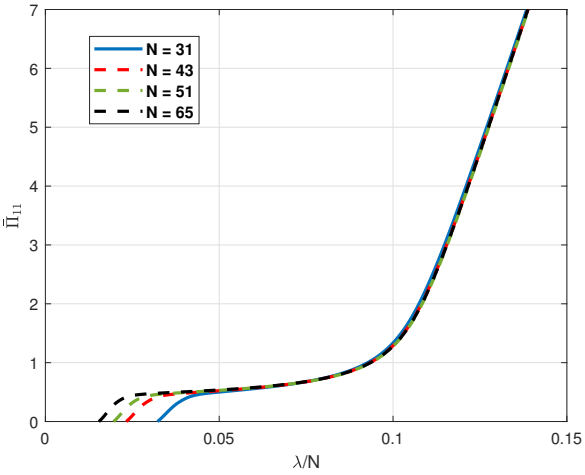

(b) Unit behavior law: $\bar{\Pi}_{11}$ as a function of λ/N

Figure 6. Influence of number of segments per chain

2.3.3 *Physically motivated identification*

To evaluate the accuracy of a hyperelastic model's prediction, we typically use a series of experimental tests. We select one of the tests to identify the model parameters, then we keep the same parameter values in the other tests to examine its predictive capability. In our case, we use the three experimental datasets from Treloar 1943 [3]:

- **Uniaxial tension**, characterized by the deformation gradient tensor

$$\mathbb{F} = \begin{bmatrix} \lambda & 0 & 0 \\ 0 & \lambda^{-1/2} & 0 \\ 0 & 0 & \lambda^{-1/2} \end{bmatrix};$$

- **Pure shear**, described by

$$\mathbb{F} = \begin{bmatrix} \lambda & 0 & 0 \\ 0 & 1 & 0 \\ 0 & 0 & \lambda^{-1} \end{bmatrix};$$

- **Equibiaxial tension**, which corresponds to

$$\mathbb{F} = \begin{bmatrix} \lambda & 0 & 0 \\ 0 & \lambda & 0 \\ 0 & 0 & \lambda^{-2} \end{bmatrix}.$$

The identification procedure is based on a physically motivated approach, relying on the specific influence of each model parameter on different phases of the mechanical response. The identification is performed in four steps:

Step 1 — Determination of the number of segments : The number of segments in the RVE is selected to match the onset of the strain-stiffening regime observed in the experimental data.

Step 2 — Identification of parameter a : The parameter a primarily affects the slope of the initial phase corresponding to chain disentanglement. It is calibrated using the small-strain region of the experimental curve.

Step 3 — Identification of parameter M_0 : The parameter M_0 controls the amplitude of the intermediate phase associated with chain unfolding. It is adjusted based on the corresponding portion of the experimental response.

Step 4 — Identification of parameter K : The parameter K governs the stiffness in the large-deformation regime and is identified using the strain-stiffening region.

Using this procedure and predefining the number of segments in the RVE $N = 260$, the identified parameters are: $a = 0.5\ rad$, $M_0 = 1.5\ 10^{-4}\ N.nm$, and $K = 3.5\ 10^{-4}\ N/nm$. The comparison with the experimental data shows (see Figure 7) that the model accurately reproduces the three loading conditions. The predictive accuracy is particularly good for large deformations ($\lambda > 2$), with moderate discrepancies observed in the small-strain region.

These results show that the proposed three-parameter model is capable of reproducing Treloar's three experimental responses for an elastomeric material. By examining the relative errors, $E = |\bar{\Pi}_{11} -$

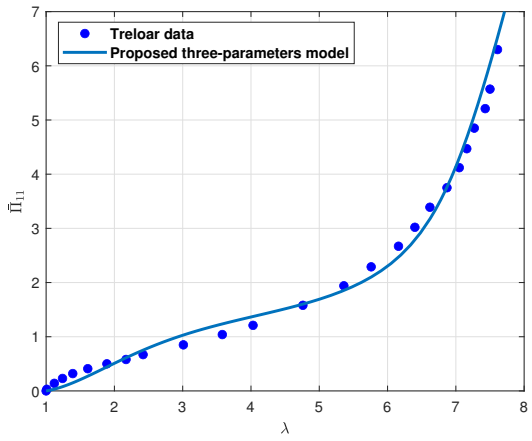

(a) Uniaxial tension

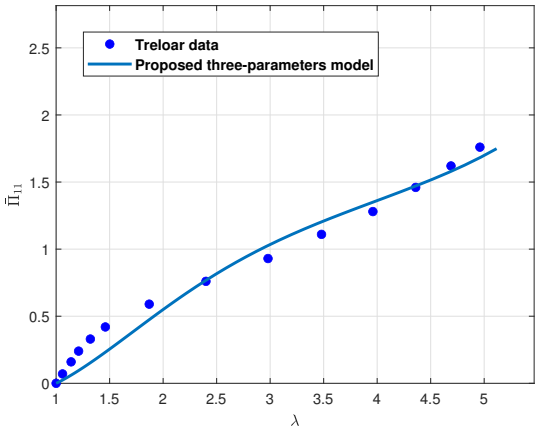

(b) Pure shear

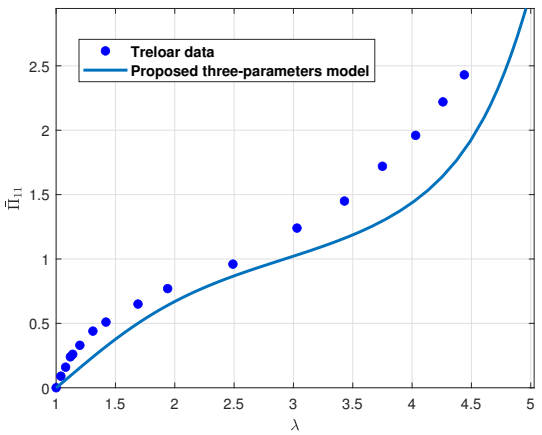

(c) Equibiaxial tension

Figure 7. Comparison between the behavior response, the first Piola–Kirchhoff stress tensor $\bar{\Pi}_{11}$ as a function of the strain gradient tensor F_{11}, with the three experiments of Treloar 1943: uniaxial tension, pure shear, and equibiaxial tension, and for $a = 0.5$ rad, $M_0 = 1.5 \times 10^{-4}$ N·nm, and $K = 3.5 \times 10^{-4}$ N/nm.

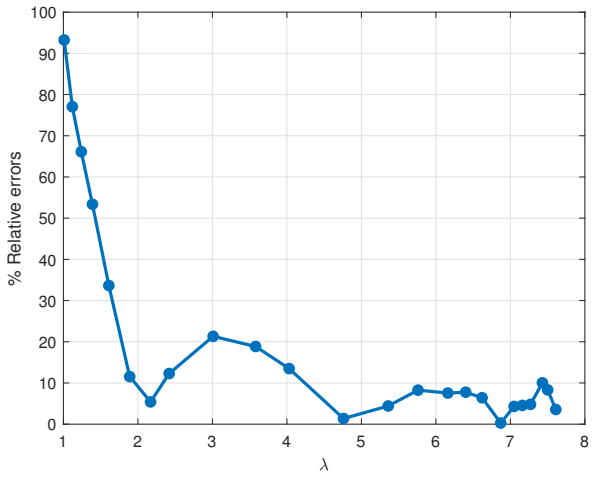

(a) Uniaxial tension

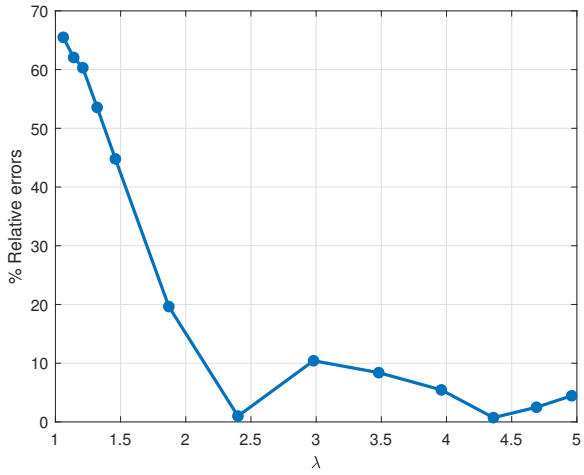

(b) Pure shear

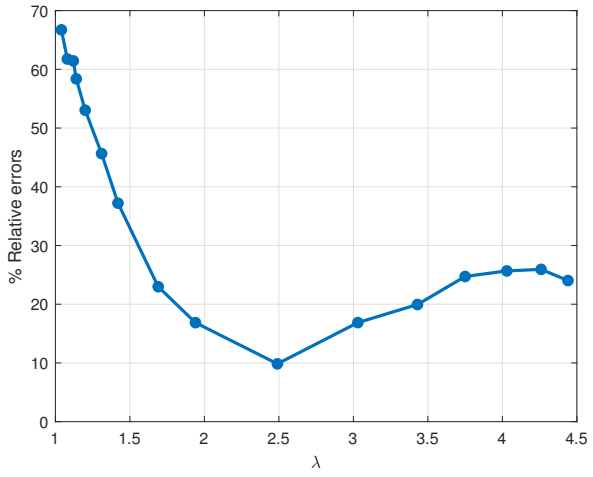

(c) Equibiaxial tension

Figure 8. Relative errors for each experimental point and for the three boundary conditions: uniaxial tension, pure shear, and equibiaxial tension.

$\bar{\Pi}_{exp}|/\bar{\Pi}_{exp}$ at each experimental point (see Figure 8), it can be observed that the predictive accuracy of the three-parameter model is highly satisfactory for deformation levels $\lambda > 2$, with maximum errors of 20% in uniaxial tension, 10% in pure shear, and 28% in equibiaxial tension. However, in the small-strain range $\lambda < 2$, the errors remain acceptable but are less satisfactory, reaching maximum values of 93% for uniaxial tension and 65% for both pure shear and equibiaxial tension.

2.3.4 *Parameter Identification Using Particle Swarm Optimization (PSO)*

a. General Principle

The proposed micromechanical approach implicitly defines a constitutive law through the solution of a system of nonlinear partial differential equations. Consequently, the proposed model does not provide an explicit relationship between the stress tensor and the strain tensor, which makes conventional identification algorithms based on the computation of the gradient of $\bar{\Pi}(\mathbb{F})$ difficult to apply in the present case. In this section, we propose the use of an algorithm capable of identifying the model parameters by minimizing the discrepancy between the numerical response of the proposed model and the experimental data, without requiring the gradient of $\bar{\Pi}(\mathbb{F})$. This algorithm is known as Particle Swarm Optimization (PSO).

The PSO algorithm employed in this work was originally introduced by James Kennedy and Russell Eberhart [35], and incorporates modifications proposed by Efrén Mezura-Montes and Carlos A. Coello Coello [27], as well as by M. E. H. Pedersen [28]. The particle swarm algorithm starts by generating an initial population of particles and assigning initial velocities to them. The objective function is then evaluated at each particle position in order to determine the best function value and the corresponding location. New velocities are subsequently computed based on the current velocity, the particles' individual best positions, and the best positions found by neighboring particles. The particle positions, velocities, and neighborhood information are iteratively updated, while ensuring that the particles remain within the prescribed bounds. The iterations continue until a stopping criterion is satisfied. Further details regarding the algorithm can be found in [30]. To couple this algorithm with the proposed three-parameter micromechanical model, we employed the **MATLAB particleswarm** function together with an objective function defined as the

normalized mean squared error in the following form:

$$J = \frac{1}{n}\sum_{i=1}^{i=n}\left(\frac{\bar{\Pi}^i_{mod} - \bar{\Pi}^i_{exp}}{max|\bar{\Pi}^i_{exp}|}\right)^2 \quad (15)$$

where n represents the number of experimental points.

b. PSO Implementation

The PSO algorithm is implemented using MATLAB's particleswarm function. The swarm size and number of iterations are selected in the range of 15–30, providing a balance between computational cost and accuracy. The default cognitive and social coefficients provided by MATLAB were used ($c_1 = 1.49$ and $c_2 = 1.49$).

c. Identification under uniaxial tension

As the first numerical simulation of this PSO algorithm, we consider the same four-chain RVE (see Figure 3). In order to determine the ranges of the three parameters a, M_0, and K, we performed two numerical tests to find the two maximum and minimum curves, above and below the uniaxial tension experimental data, which provide a range for each material parameter (see Figure 9).

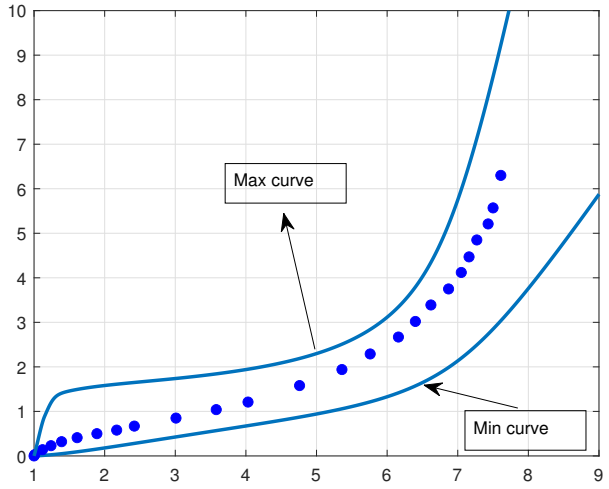

Figure 9. Pre-treatment identification, min curve: below experimental response $a = 1rad$, $M0 = 10^{-4}\ N.nm$, and $K = 1.5\ 10^{-4}\ N/nm$; max curve: above experimental response $a = 0.02rad$, $M0 = 2\ 10^{-4}\ N.nm$, and $K = 5\ 10^{-4}\ N/nm$.

This preprocessing step significantly reduces the computational cost of parameter identification by narrowing the search intervals for each parameter. As a result, a large number of particles and iterations is no longer required to determine the optimal parameters using the PSO identification procedure. Following this preprocessing stage, the parameter ranges were defined as: $a \in [0.02, 1]$, $M_0 \in [10^{-4}, 2 \times 10^{-4}]$, and $K \in [1.5 \times 10^{-4}, 5 \times 10^{-4}]$.

The optimal parameters obtained from uniaxial tension data are:

$$a = 0.6547 \text{ rad}, M_0 = 1.5884 \times 10^{-4} \text{ N} \cdot \text{nm}, \text{ and } K = 3.2580 \times 10^{-4} \text{ N/nm}.$$

The comparison between physically motivated identification and PSO-based identification (see Figures 10 and 11) shows that:

- PSO slightly improves accuracy in the intermediate and large-deformation regimes
- However, it is less accurate in the small-strain region
- The improvement remains limited when identification is performed using only uniaxial data
- This behavior is expected, as the optimization is biased toward the experimental dataset used for calibration.

By comparing the normalized mean squared error $MSN = J$ reported in Table 1, we can conclude that the PSO algorithm improves the overall accuracy in the case of uniaxial tension, while having no significant effect on the global accuracy in the cases of pure shear and equibiaxial tension. This behavior is attributed to the identification procedure, which was performed exclusively using uniaxial tension data.

d. Multi-Test Identification Strategy

To improve overall predictive performance, a multi-test identification strategy is introduced. The objective function is modified as:

$$J = w_{uni}J_{uni} + w_{sh}J_{sh} + w_{equi}J_{equi} \quad (16)$$

where J_{uni}, J_{sh}, and J_{equi} represent, respectively, the normalized mean squared error given by (15) for the cases of uniaxial tension, pure shear, and equibiaxial tension, and w_{uni}, w_{sh}, and w_{equi} are the weights associated with each experimental dataset.

This representation of the objective function allows simultaneous calibration against multiple experimental datasets, significantly improving global accuracy, particularly for pure shear and equibiaxial tension.

Table 1. Normalized mean squared error (MSN) for the two identification methods: physically motivated identification and PSO identification, for the three boundary conditions, uniaxial tension, pure shear, and equibiaxial tension.

Identification type	MSN for uniaxial tension	MSN for pure shear	MSN for equibiaxial tension	Material parameters		
				a (rad)	M_0 (N.nm)	K (N/nm)
Physically motivated identification	$1.05\ 10^{-3}$	$3.31\ 10^{-3}$	$1.44\ 10^{-2}$	0.5	$1.5\ 10^{-4}$	$3.5\ 10^{-4}$
PSO identification	$4.4275\ 10^{-4}$	$4.3657\ 10^{-3}$	$1.4247\ 10^{-2}$	0.6547	$1.5884\ 10^{-4}$	$3.2580\ 10^{-4}$

Table 2. Normalized mean squared error (MSN) for physically motivated identification in uniaxial tension, PSO identification in uniaxial tension and PSO weighted multi-test identification. For the three boundary conditions, uniaxial tension, pure shear, and equibiaxial tension.

Identification type	MSN for uniaxial tension	MSN for pure shear	MSN for equibiaxial tension	Material parameters		
				a (rad)	M_0 (N.nm)	K (N/nm)
Physically motivated identification in uniaxial tension	$1.05\ 10^{-3}$	$3.31\ 10^{-3}$	$1.44\ 10^{-2}$	0.5	$1.5\ 10^{-4}$	$3.5\ 10^{-4}$
PSO identification in uniaxial tension	$4.4275\ 10^{-4}$	$4.3657\ 10^{-3}$	$1.4247\ 10^{-2}$	0.6547	$1.5884\ 10^{-4}$	$3.2580\ 10^{-4}$
PSO weighted multi-test identification test 1	$6.0225\ 10^{-4}$	$6.9719\ 10^{-3}$	$7.4817\ 10^{-3}$	0.7994	$1.9011\ 10^{-4}$	$2.9635\ 10^{-4}$
PSO weighted multi-test identification test 2	$1.3765\ 10^{-3}$	$7.2036\ 10^{-3}$	$6.6606\ 10^{-3}$	0.7084	$1.8301\ 10^{-4}$	$3.2951\ 10^{-4}$

In Figure 12, we compare experimental results with the predictions of the proposed model obtained using different identification methods: physically motivated identification under uniaxial tension, PSO identification under uniaxial tension, and PSO-weighted multi-test identification. For the PSO-weighted multi-test identification, two sets of weights are considered:

- First test: $w_{uni} = 1/3$, $w_{sh} = 1/3$, and $w_{equi} = 1/3$
- Second test: $w_{uni} = 1/5$, $w_{sh} = 2/5$, and $w_{equi} = 2/5$

By comparing the normalized mean square errors in Table 2, we observe that the PSO-based multi-test identification significantly improves the prediction accuracy for uniaxial and equibiaxial tension tests, particularly for the case where $w_{uni} = 1/3$, $w_{sh} = 1/3$, and $w_{equi} = 1/3$.

However, although the overall accuracy improves for each test, Figure 13 shows that the proposed model still provides less accurate predictions in the small-deformation range for all three loading conditions: uniaxial tension, pure shear, and equibiaxial tension.

e. Weighted-Zone Identification

To further improve accuracy in the small-strain region, a weighted-zone strategy is introduced. The deformation domain is divided into three regions:

- Small-strain region: $\lambda \in \Omega_1 = [1, 2]$
- Intermediate (unfolding) region: $\lambda \in \Omega_2 = [2, 5.8]$,
- Large-deformation (stiffening) region: $\lambda \in \Omega_3 = [5.8, 7.6]$

In this case, we can modify the objective function by using weighting coefficients for each region. The objective function becomes:

$$J = w_1 J_1(\lambda) + w_2 J_2(\lambda) + w_3 J_3(\lambda)$$
$$\text{where} \qquad J_i(\lambda) = \frac{1}{n_i} \sum_{i \in \Omega_i} \left(\frac{\bar{\Pi}^i_{11}(\lambda) - \bar{\Pi}^i_{exp}}{max|\bar{\Pi}^i_{exp}|} \right)^2 \tag{17}$$

In Figure 14, we compare the constitutive responses obtained with the three-parameter micromechanical model using three identification methods under uniaxial tension: physically motivated identification, global PSO identification, and weighted-zone PSO identification based on Treloar's three experiments.

For the weighted-zone PSO identification, three tests were performed by progressively increasing the weight associated with the first small-deformation zone in order to improve the prediction accuracy in Ω_1. The following weight sets were considered:

- First test: $w_1 = \frac{1}{2}$, $w_2 = \frac{1}{4}$, and $w_3 = \frac{1}{4}$;
- Second test: $w_1 = \frac{3}{5}$, $w_2 = \frac{1}{5}$, and $w_3 = \frac{1}{5}$;
- Third test: $w_1 = \frac{2}{3}$, $w_2 = \frac{1}{6}$, and $w_3 = \frac{1}{6}$.

The results shown in Figure 14 indicate that increasing the weight w_1 of the first zone enables the weighted-zone PSO algorithm to identify the parameters a, M_0, and K that improve the agreement between the proposed model and Treloar's experimental results in the small-strain region for all three loading conditions: uniaxial tension, pure shear, and equibiaxial tension.

A similar trend can be observed in the pointwise error distributions shown in Figure 15. For the weight set $w_1 = \frac{2}{3}$, $w_2 = \frac{1}{6}$, and $w_3 = \frac{1}{6}$, the weighted-zone PSO algorithm improved the prediction accuracy in the small-deformation range by approximately 20% for uniaxial tension and by about 60% for pure shear and equibiaxial tension, compared with both the

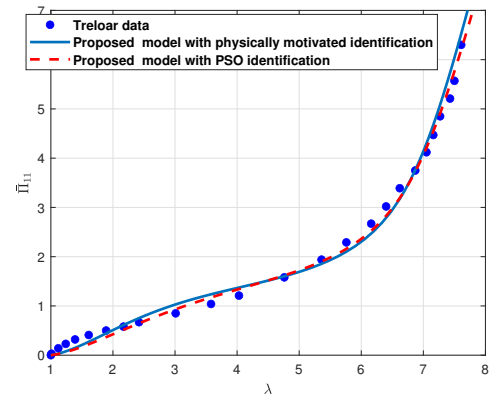

(a) Uniaxial tension

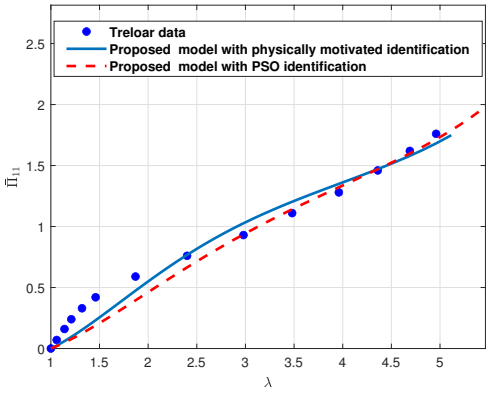

(b) Pure shear

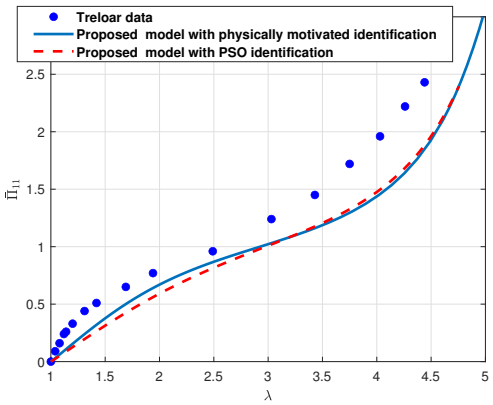

(c) Equibiaxial tension

Figure 10. Comparison of behavioral responses between Treloar's experimental results and the results obtained by the proposed three-parameter model, using two identification methods: physically motivated identification and identification by the PSO algorithm. For the three boundary conditions: uniaxial tension, pure shear, and equibiaxial tension.

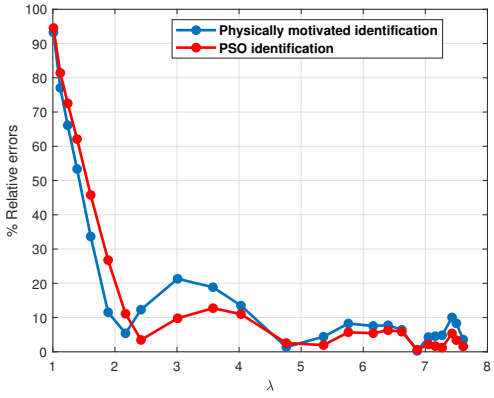

(a) Uniaxial tension

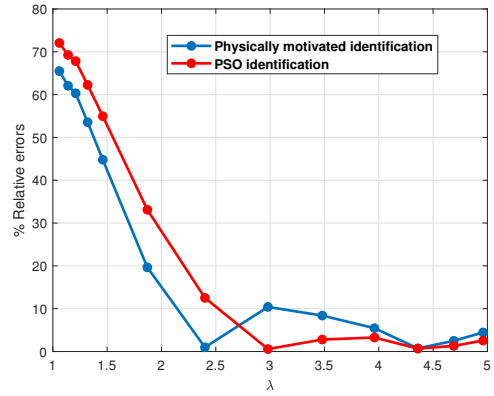

(b) Pure shear

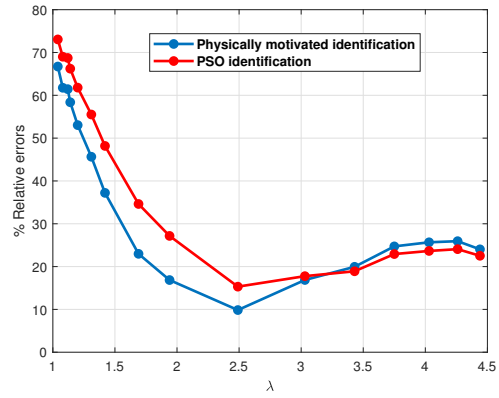

(c) Equibiaxial tension

Figure 11. Relative errors for each experimental point for the two identification methods: physically motivated identification and PSO identification, for the three boundary conditions: uniaxial tension, pure shear, and equibiaxial tension.

physically motivated identification and the global PSO identification.

However, the improvement in accuracy during the first deformation phase leads to a reduction in accuracy in the other two phases, namely the chain-unfolding phase and the stiffening phase at large deformations.

By comparing the normalized mean squared errors (MSN) in Table 3, we can also conclude that the

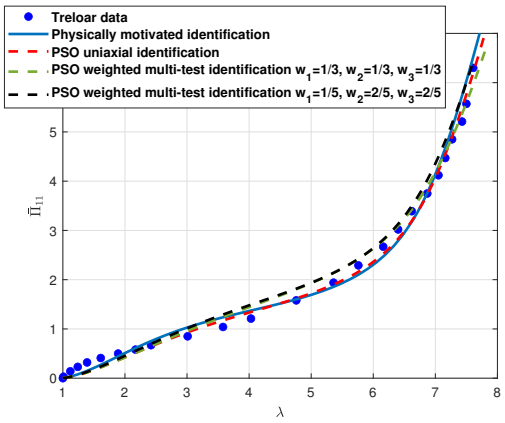

(a) Uniaxial tension

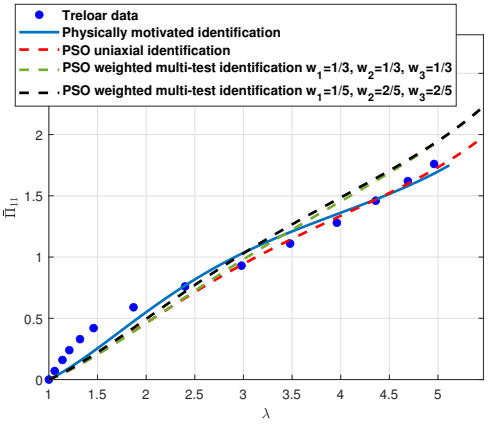

(b) Pure shear

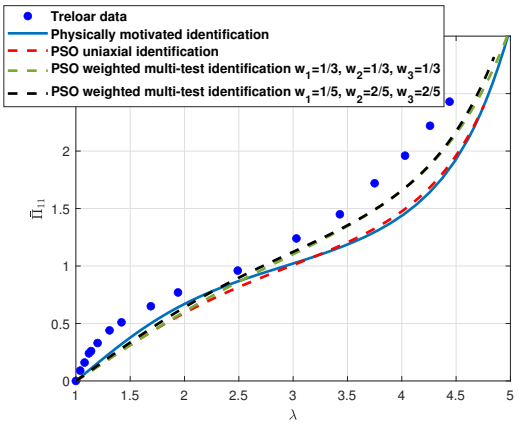

(c) Equibiaxial tension

Figure 12. Comparison of behavioral responses between Treloar's experimental results and the results obtained by the proposed three-parameter model, using physically motivated identification in uniaxial tension, PSO identification in uniaxial tension and PSO weighted multi-test identification. For the three boundary conditions: uniaxial tension, pure shear, and equibiaxial tension.

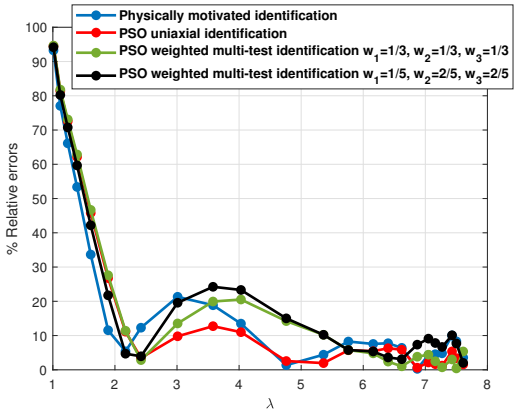

(a) Uniaxial tension

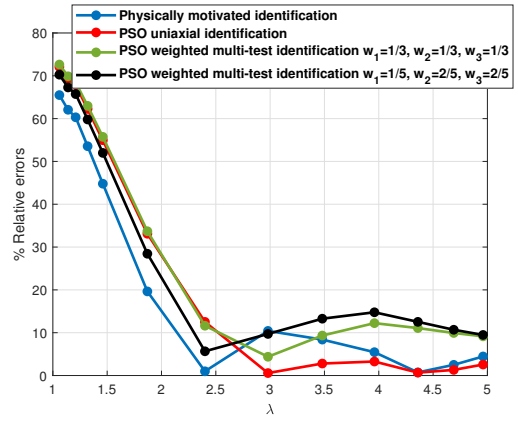

(b) Pure shear

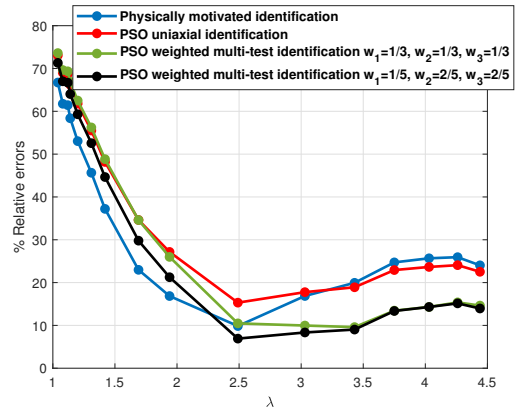

(c) Equibiaxial tension

Figure 13. Relative errors for each experimental point for physically motivated identification in uniaxial tension, PSO identification in uniaxial tension and PSO weighted multi-test identification. For the three boundary conditions, uniaxial tension, pure shear, and equibiaxial tension.

weighted-zone PSO algorithm has little influence on the overall identification accuracy for the three loading conditions: uniaxial tension, pure shear, and equibiaxial tension.

f. Combined strategy: weighted-zone and multi-test identification

We have shown that the three-test weighted PSO

Table 3. Normalized mean squared error (MSN) for the two identification methods: physically motivated identification and PSO identification, for the three boundary conditions, uniaxial tension, pure shear, and equibiaxial tension.

Identification type	MSN for uniaxial tension	MSN for pure shear	MSN for equibiaxial tension	Material parameters		
				a (rad)	M_0 (N.nm)	K (N/nm)
Physically motivated identification	$1.05\ 10^{-3}$	$3.31\ 10^{-3}$	$1.44\ 10^{-2}$	0.5	$1.5\ 10^{-4}$	$3.5\ 10^{-4}$
PSO global identification	$4.4275\ 10^{-4}$	$4.3657\ 10^{-3}$	$1.4247\ 10^{-2}$	0.6547	$1.5884\ 10^{-4}$	$3.2580\ 10^{-4}$
PSO weighted identification test 1	$1.0510\ 10^{-3}$	$3.670\ 10^{-3}$	$1.0181\ 10^{-2}$	0.3200	$1.3910\ 10^{-4}$	$3.3502\ 10^{-4}$
PSO weighted identification test 2	$3.9913\ 10^{-3}$	$1.1129\ 10^{-2}$	$3.269\ 10^{-2}$	0.1469	$1.1744\ 10^{-4}$	$3.8434\ 10^{-4}$
PSO weighted identification test 3	$3.9912\ 10^{-3}$	$1.1112\ 10^{-2}$	$3.2698\ 10^{-2}$	0.1458	$1.1682\ 10^{-4}$	$3.1574\ 10^{-4}$

algorithm accounts for the overall prediction accuracy (MSN) of the proposed model under the three loading conditions: uniaxial tension, pure shear, and equibiaxial tension. In contrast, the weighted-zone PSO algorithm provides a more accurate initial slope, allowing the constitutive law of the proposed model to reproduce the correct initial stiffness.

In this section, to further improve the efficiency of the PSO identification algorithm, we propose an objective function weighted over the three deformation zones and the three experimental tests. This new formulation aims to improve the prediction accuracy in the small-deformation range while simultaneously accounting for the three loading conditions: uniaxial tension, pure shear, and equibiaxial tension.

$$J = w_{uni}J_{uni} + w_{sh}J_{sh} + w_{equi}J_{equi} \tag{18}$$

where

$$\begin{aligned} J_{uni} &= \sum_{i=1}^{3} w_{uni}^{i} J_{uni}^{i}(\lambda), \\ J_{sh} &= \sum_{i=1}^{3} w_{sh}^{i} J_{sh}^{i}(\lambda), \\ J_{equi} &= \sum_{i=1}^{3} w_{equi}^{i} J_{equi}^{i}(\lambda) \end{aligned} \tag{19}$$

where J_{uni}, J_{sh}, and J_{equi} denote the global normalized mean squared errors defined in (15) for uniaxial tension, pure shear, and equibiaxial tension, respectively. The coefficients w_{uni}, w_{sh}, and w_{equi} represent the global weights associated with each experimental dataset.

In equation (19), $J_{uni}^{i}(\lambda)$, $J_{sh}^{i}(\lambda)$, and $J_{equi}^{i}(\lambda)$ denote the local normalized mean squared errors, while w_{uni}^{i}, w_{sh}^{i}, and w_{equi}^{i} are the local weights associated with Treloar's three experimental tests: uniaxial tension, pure shear, and equibiaxial tension. Each set of weights corresponds to one of the three deformation zones Ω_i.

In Figure 16, we compare the constitutive response obtained using several identification strategies: physically motivated identification, global PSO identification based on uniaxial tension, PSO-weighted multi-test identification using the three experimental tests, weighted-zone PSO identification, and combined weighted-zone and multi-test PSO identification using the three experimental tests.

For the combined weighted-zone and multi-test PSO algorithm, equal global weights are assigned to the three experimental datasets. For each experimental test, the deformation domain is divided into three regions: a small-deformation region, a macromolecular chain unfolding region, and a large-deformation strain-stiffening region (see Table 4).

Table 4. The three subdomains corresponding to each experimental test: uniaxial tension, pure shear, and equibiaxial tension; and the three weights used for each region: small-deformation, unfolding, and strain-stiffening under large deformation.

Test	Ω_{test}^{1}	Ω_{test}^{2}	Ω_{test}^{3}	w_{test}^{1}	w_{test}^{2}	w_{test}^{3}
Uniaxial tension	$[1, 1.6]$	$[1.6, 5.8]$	$[5.8, 7.6]$	3/5	1/5	1/5
Pure shear	$[1, 1.5]$	$[1.5, 3.5]$	$[3.5, 4.9]$	3/5	1/5	1/5
Equibiaxial tension	$[1, 1.5]$	$[1.5, 3]$	$[3, 4.4]$	3/5	1/5	1/5

By examining the pointwise errors in Figure 17 and the global errors reported in Table 5, we observe that the combined weighted-zone and multi-test PSO algorithm provides a better prediction of the initial stiffness while also improving the overall prediction accuracy for pure shear and equibiaxial tension compared with the other PSO-based algorithms. However, improving the initial slope still leads to a reduction in prediction accuracy during the second and third phases of the constitutive response predicted by the proposed model.

As a partial conclusion of this identification campaign, we observe that using the unweighted global PSO algorithm to identify the parameters a, M_0, and K of the proposed model, instead of the physically motivated identification method based on the physical influence of each parameter, does not significantly improve the prediction accuracy of the model, particularly during the initial small-deformation phase.

Table 5. Normalized mean squared error (MSN) for different identification strategies: physically motivated identification, PSO global identification, PSO weighted multi-test identification, PSO weighted-zone identification and PSO weighted-zone multi-test identification.

Identification type	MSN for uniaxial tension	MSN for pure shear	MSN for equibiaxial tension	Material parameters		
				a (rad)	M_0 (N.nm)	K (N/nm)
Physically motivated identification	$1.05\ 10^{-3}$	$3.31\ 10^{-3}$	$1.44\ 10^{-2}$	0.5	$1.5\ 10^{-4}$	$3.5\ 10^{-4}$
PSO global identification	$4.4275\ 10^{-4}$	$4.3657\ 10^{-3}$	$1.4247\ 10^{-2}$	0.6547	$1.5884\ 10^{-4}$	$3.2580\ 10^{-4}$
PSO weighted multi-test identification	$6.0225\ 10^{-4}$	$6.9719\ 10^{-3}$	$7.4817\ 10^{-3}$	0.7994	$1.9011\ 10^{-4}$	$2.9635\ 10^{-4}$
PSO weighted-zone identification	$3.9913\ 10^{-3}$	$1.1129\ 10^{-2}$	$3.269\ 10^{-2}$	0.1469	$1.1744\ 10^{-4}$	$3.8434\ 10^{-4}$
PSO weighted-zone and multi-test identification	$2.0969\ 10^{-3}$	$5.8005\ 10^{-3}$	$1.9574\ 10^{-2}$	0.1982	$1.3352\ 10^{-4}$	$3.6426\ 10^{-4}$

The PSO multi-test identification reduced the overall normalized mean squared errors (MSN) for each of Treloar's experimental tests, but it did not improve the prediction accuracy of the initial stiffness in the small-deformation range.

Using the weighted-zone PSO identification, we were able to improve the prediction accuracy in the first small-deformation phase and obtain a more accurate initial slope. However, increasing the weight associated with this phase significantly reduced the prediction accuracy in the other deformation phases, which motivated the combination of zone-weighted and test-weighted identification strategies.

This combined strategy provided a better prediction of the initial stiffness in the small-deformation range and also improved the overall MSN values for the pure shear and equibiaxial tension tests. Nevertheless, it also increased the prediction errors in the second and third phases of the constitutive response.

To achieve our objective—namely, obtaining an accurate initial stiffness in the small-deformation phase, improving the pointwise prediction accuracy throughout the three phases of the constitutive response, and reducing the overall MSN for the three experimental tests—we focus in the following section on a study aimed at understanding the limitations of the three-parameter micromechanical model.

2.3.5 *Limitations of the three-parameter micromechanical model*

The use of the weighted-zone PSO algorithm improved the prediction accuracy in the first small-deformation phase and allowed us to obtain the correct initial stiffness of the constitutive response. To better understand the limitations of the proposed three-parameter model, we now perform an additional study on the material parameters while keeping the initial stiffness of the model fixed.

The micromechanical elements governing the first and second phases of the constitutive response in the proposed micromechanical approach are spiral springs. According to equation (3), their initial stiffness is defined by the ratio M_0/a. In this study, the parameters a and M_0 are varied progressively while maintaining the optimal initial stiffness value fixed, given by $\frac{M_0}{a} = \frac{1.1682\ 10^{-4}\ N.nm}{0.1458\ rad} = 8.0123\ 10^{-4}\ N.nm/rad$, which was identified using the weighted-zone PSO algorithm (see Table 3, test 3, in § *2.3.4-e*).

The linear elastic springs become active only after the complete unfolding of all macromolecular chain segments, corresponding to the stiffening phase at large deformations. Therefore, the stiffness parameter K associated with these linear springs was set at $3.1574\ 10^{-4}\ N/nm$ for all tests of the present study.

Table 6. Material parameter values a, M_0, and K for each test.

tests	Material parameters		
	a (rad)	M_0 (N.nm)	K (N/nm)
test 1	0.1872	$1.5\ 10^{-4}$	$3.1574\ 10^{-4}$
test 2	0.1747	$1.4\ 10^{-4}$	$3.1574\ 10^{-4}$
test 3	0.1498	$1.2\ 10^{-4}$	$3.1574\ 10^{-4}$
test 4	0.1248	$1\ 10^{-4}$	$3.1574\ 10^{-4}$
test 5	0.0998	$0.8\ 10^{-4}$	$3.1574\ 10^{-4}$
test 6	0.0749	$0.6\ 10^{-4}$	$3.1574\ 10^{-4}$

In Figure 18, we present the numerical tests performed by varying the parameters a and M_0 within the proposed three-parameter micromechanical model (see Table 6).

We observe that, regardless of the values of a and M_0, fixing the initial stiffness ratio of the spiral springs, M_0/a, keeps the initial slope of the macroscopic constitutive law $\bar{\Pi}_{11} = f(\lambda)$ unchanged. We also note that the proposed approach is consistently able to reproduce the three characteristic phases of the hyperelastic behavior of elastomers using only the three parameters a, M_0, and K.

However, when comparing the experimental and numerical responses obtained with the proposed three-parameter model, we find that the shapes of phase 1 (concave region) and phase 3 (nearly linear stiffening region) are well reproduced. In contrast, phase 2 of the numerical response exhibits a plateau with an almost constant stress level for all six tests.

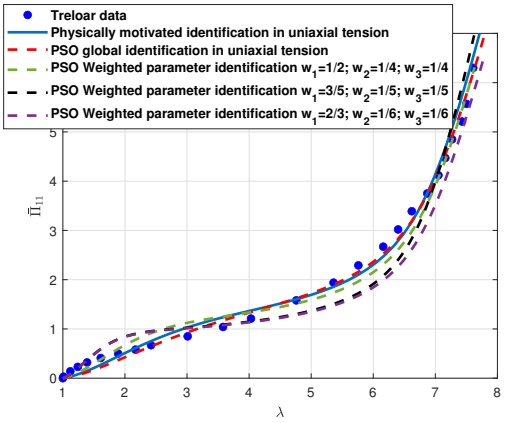

(a) Uniaxial tension

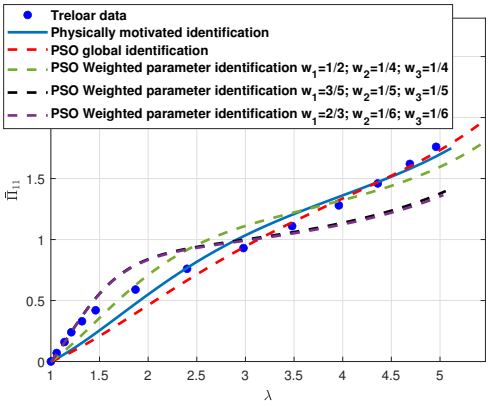

(b) Pure shear

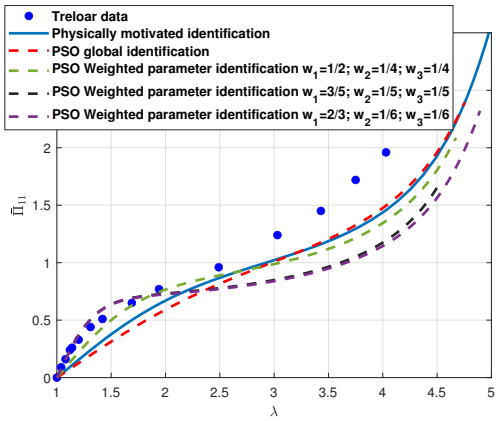

(c) Equibiaxial tension

Figure 14. Behavior responses: Treloar's experimental results and the results obtained by the proposed three-parameter model, using physically motivated identification, PSO global identification and PSO weighted-zone identification. For the three boundary conditions: uniaxial tension, pure shear, and equibiaxial tension.

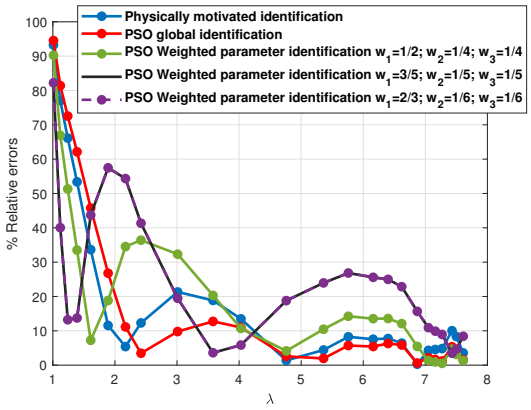

(a) Uniaxial tension

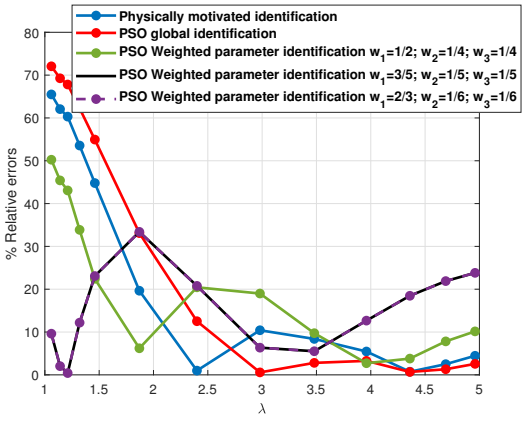

(b) Pure shear

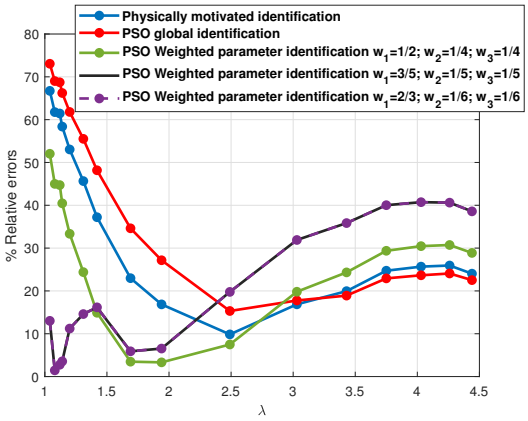

(c) Equibiaxial tension

Figure 15. Relative errors for each experimental point for the three identification methods: physically motivated identification, PSO global identification and PSO weighted-zone identification, for the three boundary conditions, uniaxial tension, pure shear, and equibiaxial tension.

This behavior is not observed experimentally, where phase 2 instead corresponds to a progressive increase in stress during deformation.

This stress stabilization can be explained by the use of sigmoidal spiral spring elements, which produce stabilization of the bending moment at the value M_0 during the unfolding of the macromolecular chain

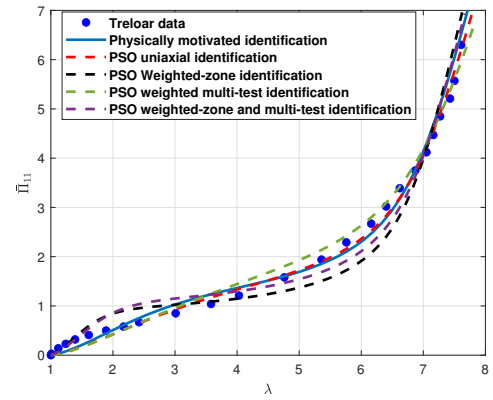

(a) Uniaxial tension

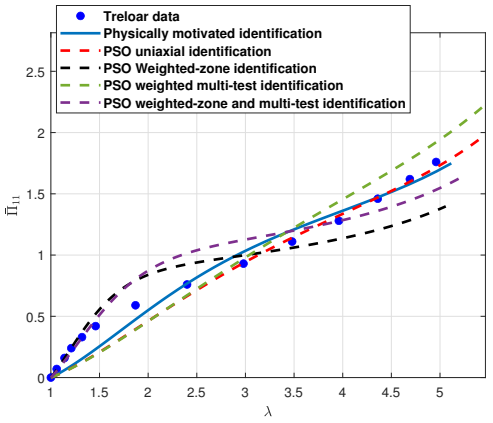

(b) Pure shear

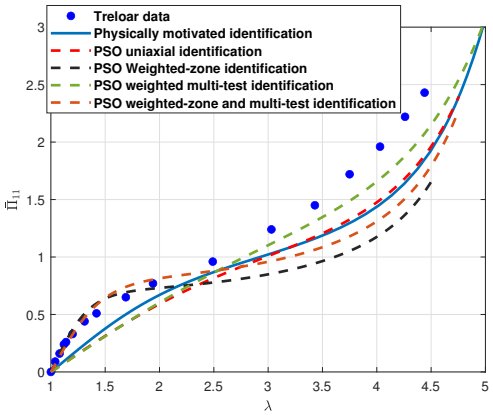

(c) Equibiaxial tension

Figure 16. Behavior responses: Treloar's experimental results and the results obtained by the proposed three-parameter model, using different identification strategies: physically motivated identification, PSO global identification, PSO weighted multi-test identification, PSO weighted-zone identification and PSO weighted-zone multi-test identification. For the three boundary conditions: uniaxial tension, pure shear, and equibiaxial tension.

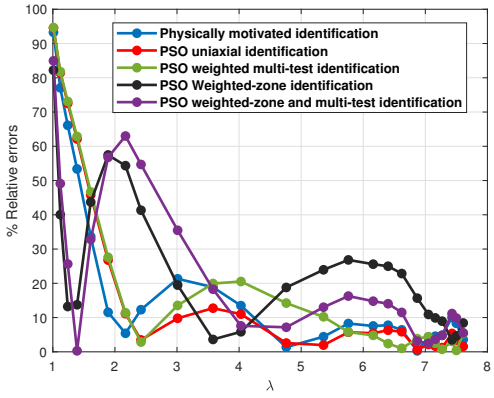

(a) Uniaxial tension

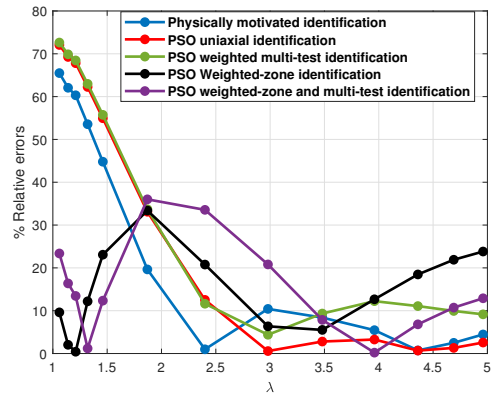

(b) Pure shear

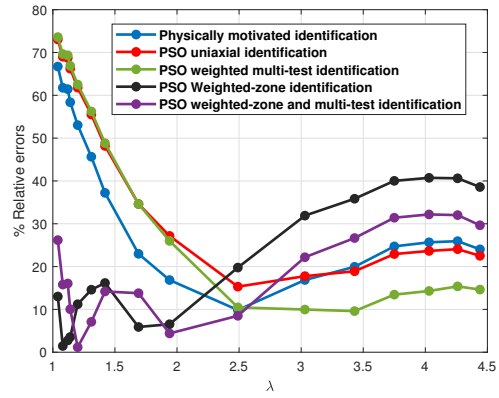

(c) Equibiaxial tension

Figure 17. Relative errors for each experimental point for different identification strategies: physically motivated identification, PSO global identification, PSO weighted multi-test identification, PSO weighted-zone identification and PSO weighted-zone multi-test identification.

segments without additional resistance stiffness (see Figure 2). As a result, the second phase of the macroscopic constitutive law is associated with an almost constant stress level.

The discrepancy in stress evolution between the experimental and numerical responses makes it difficult for the model to accurately reproduce phase 2 while preserving the correct initial slope of the

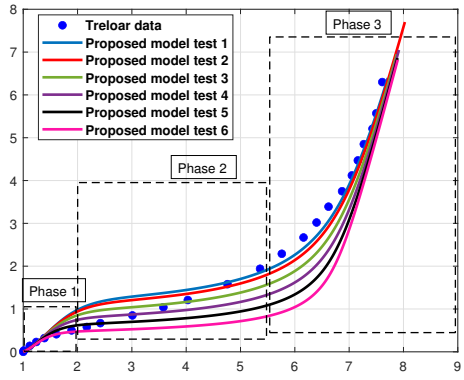

Figure 18. Behavioral law established by the three-parameter model proposed, for a fixed $\frac{M_0}{a} = \frac{1.1682\ 10^{-4}\ N.nm}{0.1458\ rad} = 8.0123\ 10^{-4}\ N.nm/rad$ while varying a and M_0.

macroscopic constitutive law. Consequently, the prediction accuracy of phase 2, as well as that of the subsequent phase 3, is reduced, as observed in the previous studies.

The analyses performed in this section provide a comprehensive understanding of both the advantages and the limitations of the proposed three-parameter model. In the next section, we introduce an extended model, based on the same micromechanical approach, designed to overcome the limitations of the three-parameter formulation.

3 Extended four-parameter micromechanical model for the hyperelastic behavior of elastomers

3.1 Description of the extended model

In this section, we propose an extended version of the three-parameter model to improve the prediction accuracy of the proposed micromechanical approach. We consider a Representative Volume Element (RVE) of an elastomer composed of M macromolecular chains. Each chain C_k consists of n_k linear elastic springs connected to n_k nonlinear elastic spiral springs. According to previous studies, the spiral springs govern the first and second phases of the constitutive response, while the linear elastic springs become active after the unfolding of the macromolecular chain segments during the third phase.

In this formulation, the same tensile deformation energy $w_{t_i}^k\left(\Delta l_i^k\right)$ is retained for the elastic springs, as defined in equation (1). For the nonlinear spiral springs, we propose the following nonlinear relationship between the bending moment M_i^k and the angular variation $\Delta\varphi_i^k$:

$$M_i^k\left(\Delta{\varphi_i}^k\right) = M_0 \cdot \tanh\left(\frac{\Delta\varphi_i^k}{a}\right) + b\Delta\varphi_i^k \qquad (20)$$

corresponds to a bending strain energy $w_{b_i}^k$ in the following form:

$$w_{b_i}^k\left(\Delta{\varphi_i}^k\right) = a{\cdot}M_0{\cdot}\ln\left(\cosh\left(\frac{\Delta\varphi_i^k}{a}\right)\right) + \frac{1}{2}.b.\left(\Delta\varphi_i^k\right)^2 \qquad (21)$$

The linear stiffness parameter b in the extended model (20) is introduced to account for the increase in stress associated with the complete unfolding of the segments of macromolecular chains.

In Figure 19, we present the nonlinear behavior of the spiral springs, namely the evolution of the bending moment M_i^k as a function of the angular variation $\Delta\varphi_i$.

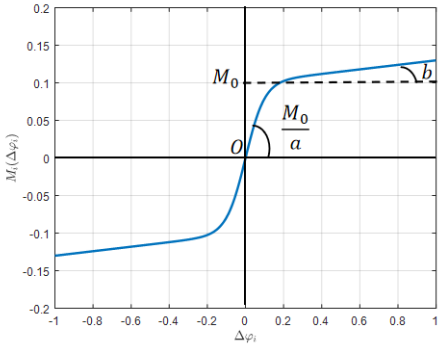

Figure 19. Nonlinear behavior of the spiral springs: the moment M_i as a function of the variation of the angles $\Delta\varphi_i$, for $a = 0.1$, $M_0 = 0.1$, $b = 0.03$.

Unlike the original three-parameter model, which stabilizes after the unfolding of the macromolecular chain segments without exhibiting additional stiffness—thereby producing an almost constant stress during the second phase of the macroscopic constitutive response—the extended model maintains a small residual stiffness b after chain unfolding. This additional stiffness makes it possible to reproduce the progressive increase in stress observed experimentally during the second phase of the constitutive response.

The extended model is characterized by four parameters: a, b, M_0, and K, which represent, respectively, the bending angle parameter, the residual stiffness at the end of bending, the maximum bending moment of the spiral springs, and the linear stiffness of the elastic springs.

It should also be noted that when $b = 0$, the extended formulation reduces to the original three-parameter model.

The expressions of the total deformation energy and the potential energy of the RVE given in (4), as well as the subsequent derivations and solving algorithms, remain unchanged from those presented in sections *2.1* and *2.2*.

3.2 Remarks on the physical significance of the model parameters

To better explain the role of each of the four parameters and analytically highlight their influence on the overall behavior of a macromolecular chain, we present in this section a limiting analysis of the energy expressions in the different deformation phases.

Before alignment of the macromolecular chain segments, the mechanical response is governed solely by the spiral springs. In this regime, two limiting cases can be identified.

In the small-strain limit, corresponding to deformations close to the undeformed configuration, $\Delta\varphi_i^k \to 0$, the strain energy reduces to the quadratic form:

$$E_p\left(l_i^k, \varphi_i^k\right) \sim \frac{1}{2}\left(\frac{M_0}{a} + b\right) \sum_{k=1}^{M} \sum_{i=1}^{n_k} \left(\Delta\varphi_i^k\right)^2 \qquad (22)$$

where $\left(\frac{M_0}{a} + b\right)$ represents the initial stiffness.

In contrast, at large deformations associated with the unfolding of the macromolecular chain segments, the asymptotic response is mainly governed by the stiffness parameter b. In this case, the strain energy takes the form:

$$E_p\left(l_i^k, \varphi_i^k\right) \sim \frac{1}{2}.b \sum_{i=1}^{n_k} \left(\Delta\varphi_i^k\right)^2 \qquad (23)$$

In the stiffening regime, corresponding to the complete alignment of the macromolecular chain segments, the mechanical response is governed exclusively by the longitudinal springs. The strain energy then asymptotically becomes:

$$E_p\left(l_i^k, \varphi_i^k\right) \sim \frac{1}{2}.K \sum_{i=1}^{n_k} \left(\Delta l_i^k\right)^2 \qquad (24)$$

where the parameter K controls the macroscopic stiffness of the material in the large-deformation regime.

3.3 Numerical Results and Discussion

3.3.1 Influence of four-parameter model a, b, M_0, and K

To highlight the differences between the extended model and the original three-parameter model, we performed an additional study on the influence of the four parameters a, b, M_0, and K in the new formulation. Four numerical tests were carried out using the same four-chain RVE (see Figure 3). In each test, three parameters were kept constant while the fourth parameter was varied.

- First test: parameter a was varied while fixing $b = 5 \times 10^{-5}$ N · nm, $M_0 = 1.5 \times 10^{-4}$ N · nm, and $K = 3.5 \times 10^{-4}$ N/nm.
- Second test: parameter M_0 was varied while fixing $a = 0.05$ rad, $b = 5 \times 10^{-4}$ N · nm, and $K = 3.5 \times 10^{-4}$ N/nm.
- Third test: parameter K was varied while fixing $a = 0.05$ rad, $b = 5 \times 10^{-4}$ N · nm, and $M_0 = 0.6 \times 10^{-4}$ N · nm.
- Fourth test: parameter b was varied while fixing $a = 0.05$ rad, $M_0 = 0.6 \times 10^{-4}$ N · nm, and $K = 3.5 \times 10^{-4}$ N/nm.

In Figure 20, we present the macroscopic constitutive responses obtained for the four tests, namely the first Piola–Kirchhoff stress as a function of the macroscopic deformation gradient. We observe that the influence of the three original parameters a, M_0, and K remains unchanged. Parameter a still controls the slope of the first phase associated with the disentanglement of the macromolecular chains, parameter M_0 influences the amplitude of the first and second phases related to the unfolding of the macromolecular chain segments, and parameter K governs the slope of the third stiffening phase at large deformations. In addition, the new parameter b introduced in the extended model makes it possible to control the slope of the second phase of the constitutive response without affecting the initial stiffness of the model. This was not achievable with the original three-parameter model. As a result, the extended formulation provides greater flexibility and is better suited for fitting a wide range of experimental data.

3.3.2 Validation of the extended model

In order to validate the extended four-parameter model, we compare it with Treloar's experimental results.

We identify the four parameters a, b, M_0, and K on Treloar's three experimental tests with weighting

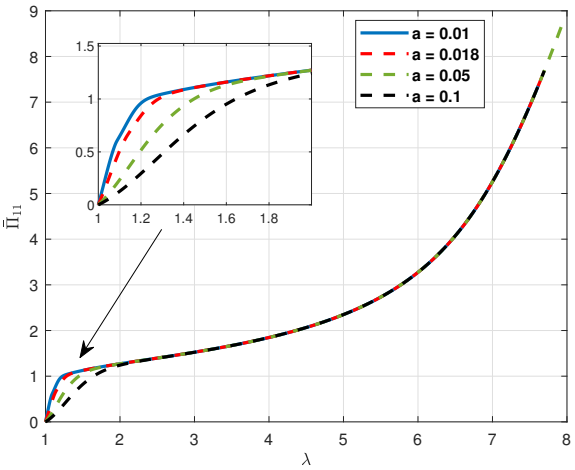

(a) Influence of parameters a for $b = 5\ 10^{-5}\ N.nm$, $M_0 = 1.5\ 10^{-4}\ N.nm$, and $K = 3.5\ 10^{-4}\ N/nm$

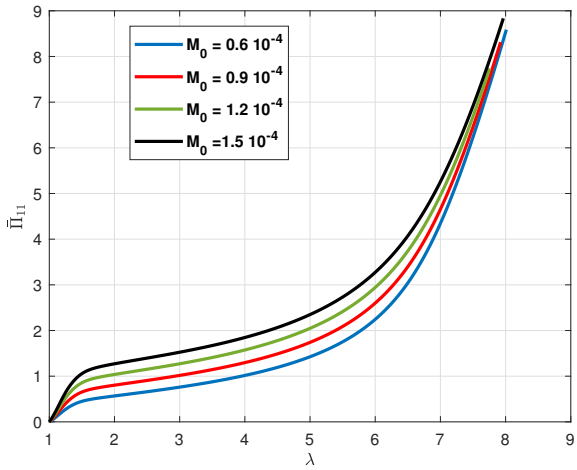

(b) Influence of parameters M_0 for $a = 0.05\ rad$, $b = 5\ 10^{-4}\ N.nm$, and $K = 3.5\ 10^{-4}\ N/nm$

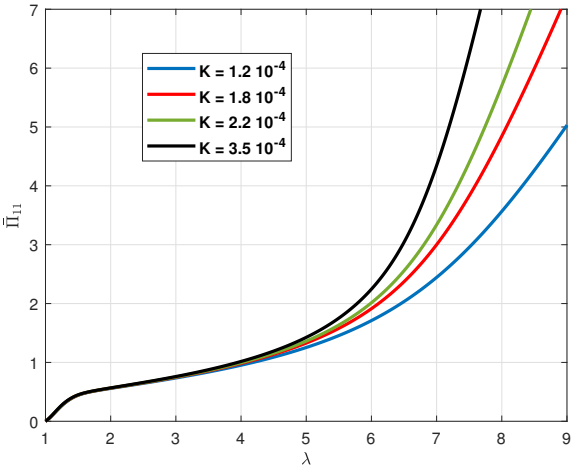

(c) Influence of parameters K for $a = 0.05\ rad$, $b = 5\ 10^{-4}\ N.nm$, and $M_0 = 0.6\ 10^{-4}\ N.nm$

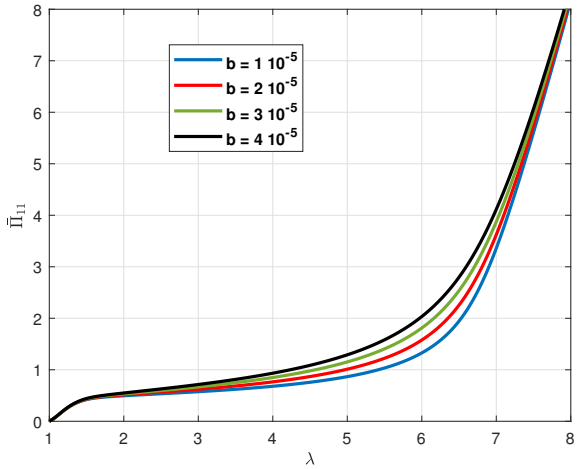

(d) [Influence of parameters b for $a = 0.05\ rad$, $M_0 = 0.6\ 10^{-4}\ N.nm$, and $K = 3.5\ 10^{-4}\ N/nm$

Figure 20. Influence of the four material parameters a, M_0, K, and b of the proposed micromechanical model.

Table 7. Normalized mean squared error (MSN) for the two models and for the three boundary conditions, uniaxial tension, pure shear, and equibiaxial tension.

Identification type	MSN for uniaxial tension	MSN for pure shear	MSN for equibiaxial tension	Material parameters			
				a (rad)	M_0 (N.nm)	K (N/nm)	b (N.nm)
Three-parameter model	$2.0969\ 10^{-3}$	$5.8005\ 10^{-3}$	$1.9574\ 10^{-2}$	0.1982	$1.3352\ 10^{-4}$	$3.6426\ 10^{-4}$	–
Four-parameter model	$1.1074\ 10^{-3}$	$1.0887\ 10^{-3}$	$3.0693\ 10^{-3}$	0.0856	$6.5062\ 10^{-5}$	$2.5154\ 10^{-4}$	$8.9195\ 10^{-5}$

applied to the three phases of each constitutive response using the fourth identification strategy that we presented in the previous section, the PSO weighted-zone and multi-test identification, in order to find the most optimal parameters of the proposed model. The parameter values identified by the PSO weighted-zone and multi test algorithm are:

$$a = 0.0856, b = 8.9195\ 10^{-5}\ N.nm,$$
$$M_0 = 6.5062\ 10^{-5}\ N.nm, \text{ and } K = 2.5154\ 10^{-4}\ N/nm.$$

In Figure 21, we present a comparison between the constitutive response established by the three- and four-parameter proposed model, and the experimental results. We observe that the proposed four-parameter model makes it possible to fit the three phases with a good initial slope for the three experimental Treloar responses: uniaxial tension (see Figure 21(a)), pure shear (see Figure 21(b)), and equibiaxial tension (see Figure 21(c)). We can also note that parameter b contributes additional resistance in the second phase,

thus producing a stress evolution during deformation similar to Treloar's experimental response, which is not observed in the response of the three-parameter model. This flexibility in fitting the second phase, achieved by adding a fourth parameter b without changing the initial stiffness of the behavior law, allows the overall responses (three phases) of the proposed four-parameter model to better approximate the three experimental results.

By examining the pointwise errors shown in Figure 22, we observe that the four-parameter model provides very satisfactory prediction accuracy for the three loading conditions: uniaxial tension (Figure 22(a)), pure shear (Figure 22(b)), and equibiaxial tension (Figure 22(c)). The extended model significantly improves the accuracy of the proposed micromechanical approach in uniaxial tension. The prediction error is reduced by approximately 5% in the small-deformation range and by nearly 40% in the intermediate phase of the constitutive response. In the final strain-stiffening phase at large deformations, the model maintains the same relative error level as the three-parameter model, which remains below 18%. For the pure shear test, the extended model significantly improves the prediction accuracy over all three phases of the constitutive response, with a maximum error of about 8%. For the equibiaxial tension test, the four-parameter model improves the prediction accuracy by approximately 15% in the initial small-deformation phase and by nearly 20% in the final large-deformation hardening phase.

From an overall point of view, in Table 7 we compare the normalized mean squared error (MSN) for the three Treloar boundary conditions. We can conclude that the extended four-parameter model significantly improves the normalized mean squared error (MSN), particularly in the case of pure shear and equibiaxial tension.

Based on the results in Figure 21, Figure 22, and Table 7, we can conclude that the extended four-parameter model coupled with PSO weighted-zone and multi-test identification provides a numerical response of the behavior law characterized by good initial stiffness (see Figure 21), good local prediction accuracy at each experimental point (see Figure 22), and good overall error (MSN) for the experimental tests: uniaxial tension, pure shear, and equibiaxial tension (Table 7).

In order to evaluate the proposed four-parameter model in more detail, we perform another comparison with some classical models based on the statistical

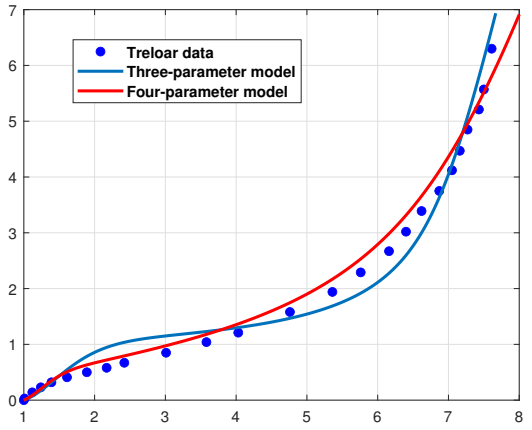

(a) Uniaxial tension

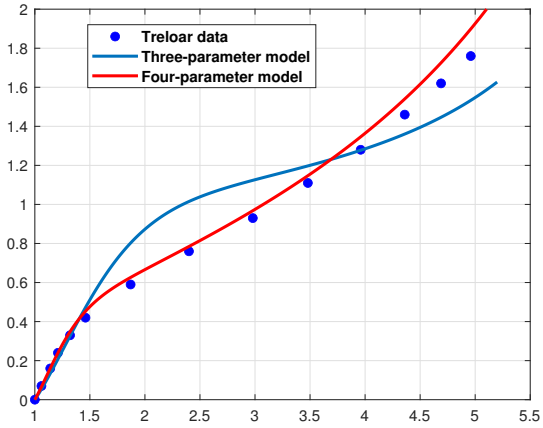

(b) Pure shear

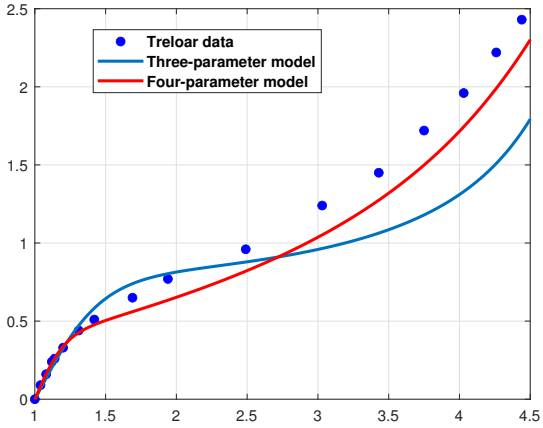

(c) Equibiaxial tension

Figure 21. Behavior responses: Treloar's experimental results and the results obtained by the proposed three and four parameter models, using PSO weighted-zone and multi test identification. For the three boundary conditions: uniaxial tension, pure shear, and equibiaxial tension.

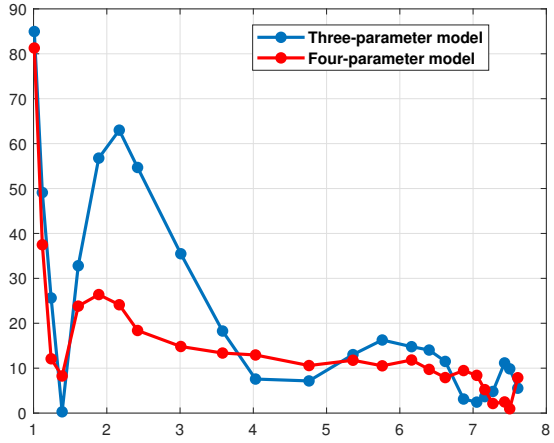

(a) Uniaxial tension

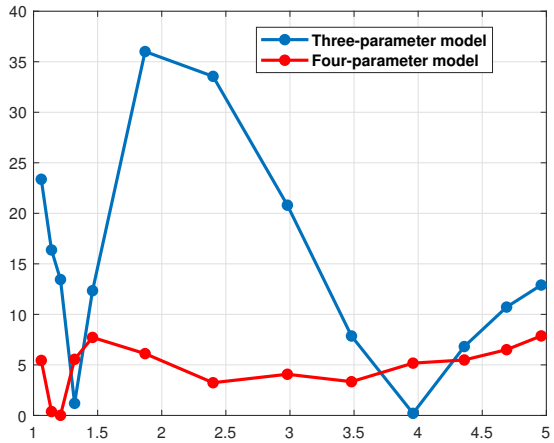

(b) Pure shear

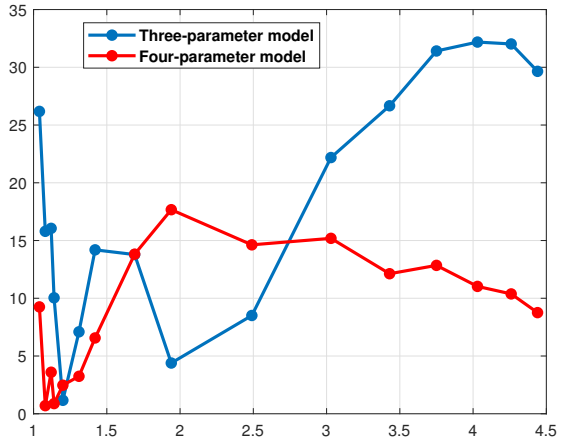

(c) Equibiaxial tension

Figure 22. Relative errors for each experimental point for the proposed three and four parameters models using PSO weighted-zone and multi test identification.

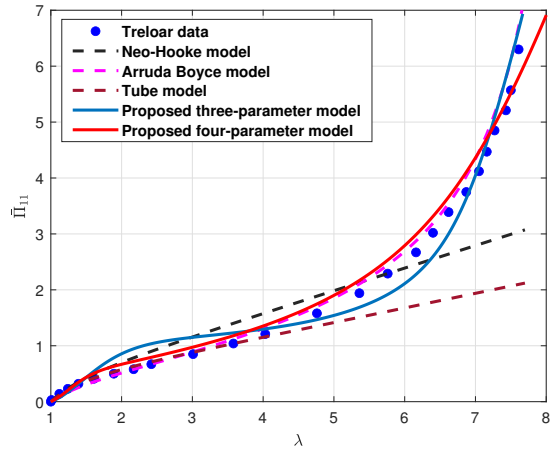

(a) Uniaxial tension

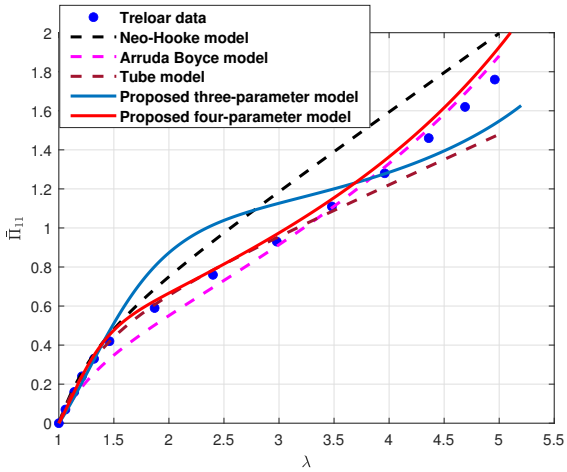

(b) Pure shear

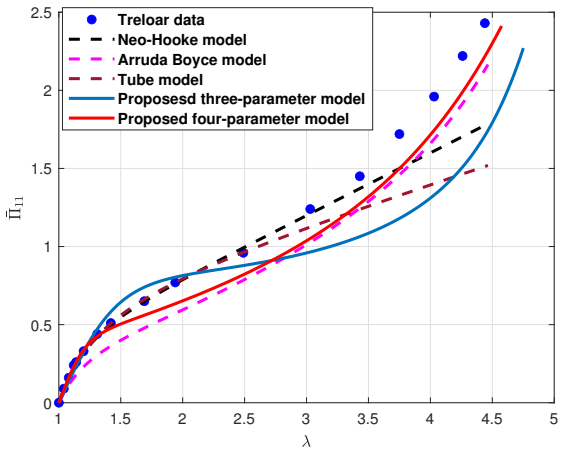

(c) Equibiaxial tension

Figure 23. Comparison of the proposed three-parameters-model, four-parameters-model, Treloar's experimental results and statistical models, for three boundary conditions : uniaxial tension, pure shear and equibiaxial tension.

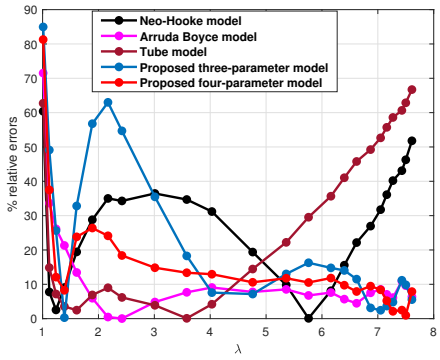

(a) Uniaxial tension

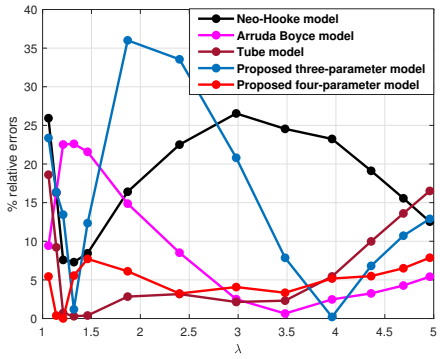

(b) Pure shear

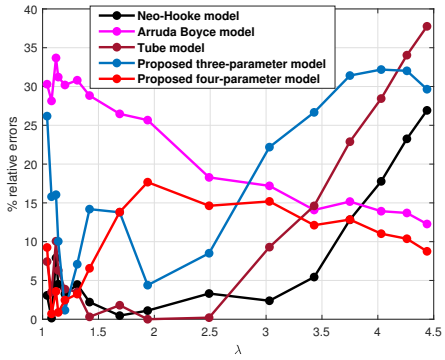

(c) Equibiaxial tension

Figure 24. Relative errors for each experimental point for the proposed four-parameters model, three-parameters model and statistical models, for the three boundary conditions, uniaxial tension, pure shear, and equibiaxial tension.

approach reported in the literature. The models chosen are: the neo-Hookean model [3], the Arruda Boyce model [7], and the Tube model [36]. For the parameter values of each model, we used the values identified in [37] and [38]. These values are presented in Table 8.

In Figure 23, we compare all the constitutive responses established by: the four-parameter model, the three-parameter model and statistical models. We note

Table 8. Parameters identified from Treloar's (1943) experimental data [38], [37].

Model	Parameters
Néo-Hookean	$\frac{1}{2}knT = 0.2\ MPa$
Arruda Boyce	$C_r = 0.30\ MPa, N = 25.9$
Tube	$G_c = 0.266\ MPa, G_e = 0.111\ MPa, \beta = 0.375$

that the proposed three and four-parameter models are capable of reproducing the three phases that characterize the hyperelastic behavior of elastomers similarly to the Arruda Boyce model (see Figure 23(a)). However, Neo-Hookean and Tube models are unable to reproduce the ascending concavity of the second phase and the entirety of the third phase of stiffening under high deformations, as several models in the literature require several parameters (up to 9 parameters) to obtain these three phases of behavior observed experimentally.

By also comparing the errors relative to each experimental point in Figure 24 for the three boundary conditions, we can conclude that the prediction accuracy of the proposed four-parameter model is very satisfactory in three cases, uniaxial tension (Figure 24-a), pure shear (Figure 24(b)) and equibiaxial tension (Figure 24(c)) compared with the statistical models. We can also consider that the accuracy of the predictions of the three-parameter model is reasonable compared to the neo-Hookean and the Tube models.

In this study, the response of the proposed micromechanical model, formulated within a two-dimensional RVE under the plane stress assumption, is compared with three experimental datasets reported by L. R. G. Treloar (1944). These experiments were conducted on thin rubber specimens subjected to uniaxial tension, planar tension (commonly referred to as pure shear), and equibiaxial tension.

Although the plane stress assumption provides a reasonable approximation for such thin structures, a fully three-dimensional formulation would more accurately capture the actual mechanical response of elastomers under these loading conditions.

4 Conclusions

In this work, we developed a new four-parameter model to describe the hyperelastic behavior of elastomers. This model extends and improves the three-parameter micromechanical approach previously proposed in [1, 2]. At the microscale, each

macromolecular chain is modeled by linear springs connected through nonlinear spiral springs. The nonlinear behavior of the spiral springs is represented by the combination of a sigmoidal threshold function, describing the activation of rotations during the initial disentanglement of the macromolecular chains, and a linear function accounting for the residual stiffness during the unfolding of chain segments. This new formulation provides greater flexibility and significantly improves the agreement between numerical predictions and experimental observations.

The equilibrium problem is obtained by minimizing the total potential energy, defined as the sum of the energies stored in the linear and spiral springs. The constitutive response of the model is established implicitly by solving the resulting system of nonlinear equilibrium equations. To reduce the computational cost, the nonlinear problem was solved using the Asymptotic Numerical Method (ANM).

Several numerical simulations were carried out on a representative volume element (RVE) composed of four chains connected at a central junction. These simulations were used to analyze the limitations of the three-parameter model and to demonstrate the robustness and advantages of the proposed four-parameter formulation.

The three-parameter model was first compared with the experimental results reported by L. R. G. Treloar using two identification approaches: a physically motivated identification based on the physical role of each parameter, and several PSO-based identification strategies aimed at minimizing the discrepancy between numerical and experimental responses. The results showed that improving the initial stiffness prediction generally reduced the prediction accuracy in the second and third deformation phases.

In contrast, the proposed four-parameter model demonstrated a much greater flexibility in fitting Treloar's experimental data. The model provided accurate predictions for the three deformation phases and for the three loading conditions considered: uniaxial tension, pure shear, and equibiaxial tension. The obtained results also compare favorably with the original three-parameter model and several classical statistical constitutive models.

As a perspective, the proposed four-parameter formulation will be extended to a fully three-dimensional framework in order to provide a more realistic representation of the mechanical response of elastomeric materials. Future work will also focus on incorporating additional micromechanical mechanisms into the formulation to better describe the microscopic physical phenomena governing the macroscopic constitutive response. Finally, we aim to optimize the choice of weights used in the different PSO-based identification strategies by employing machine learning techniques, particularly neural-network-based approaches.

Data Availability Statement

Data will be made available on request.

Funding

This work was supported without any funding.

Conflicts of Interest

The authors declare no conflicts of interest.

AI Use Statement

The authors declare that no generative AI was used in the preparation of this manuscript.

Ethical Approval and Consent to Participate

Not applicable.

References

[1] Ouardi, A., Boukamel, A., & Damil, N. (2023). A model for hyperelastic rubber-like materials based on micro-mechanical elements. *European Journal of Mechanics-A/Solids, 101*, 105036. [CrossRef]

[2] Ouardi, A., Hamdaoui, A., Arfaoui, M., Boukamel, A., & Damil, N. (2025). A 3D micromechanical model for hyperelastic rubber-like materials and its numerical resolution by the Asymptotic Numerical Method (ANM). *European Journal of Mechanics-A/Solids, 111*, 105594. [CrossRef]

[3] Treloar, L. R. (1943). The elasticity of a network of long-chain molecules—II. *Transactions of the Faraday Society, 39*, 241-246. [CrossRef]

[4] Khiêm, V. N., Le Cam, J. B., Charles, S., & Itskov, M. (2022). Thermodynamics of strain-induced crystallization in filled natural rubber under uni-and biaxial loadings, Part I: Complete energetic characterization and crystallinity evaluation. *Journal of the Mechanics and Physics of Solids, 159*, 104701. [CrossRef]

[5] Flory, P. J. (1947). Thermodynamics of crystallization in high polymers. I. Crystallization induced by

stretching. *The Journal of Chemical Physics, 15*(6), 397-408. [CrossRef]

[6] Gent, A. N., Kawahara, S., & Zhao, J. (1998). Crystallization and strength of natural rubber and synthetic cis-1, 4-polyisoprene. *Rubber Chemistry and technology, 71*(4), 668-678. [CrossRef]

[7] Arruda, E. M., & Boyce, M. C. (1993). A three-dimensional constitutive model for the large stretch behavior of rubber elastic materials. *Journal of the Mechanics and Physics of Solids, 41*(2), 389-412. [CrossRef]

[8] Ogden, R. W., Saccomandi, G., & Sgura, I. (2004). Fitting hyperelastic models to experimental data. *Computational mechanics, 34*(6), 484-502. [CrossRef]

[9] Bischoff, J. E., Arruda, E. A., & Grosh, K. (2002). A microstructurally based orthotropic hyperelastic constitutive law. *Journal of applied mechanics, 69*(5), 570-579. [CrossRef]

[10] Bischoff, J. E., Arruda, E. M., & Grosh, K. (2002). Orthotropic Hyperelasticity in Terms of an Arbitrary Molecular Chain Model. *Journal of Applied Mechanics, 69*(2), 198-201. [CrossRef]

[11] Kuhl, E., Garikipati, K., Arruda, E. M., & Grosh, K. (2005). Remodeling of biological tissue: mechanically induced reorientation of a transversely isotropic chain network. *Journal of the Mechanics and Physics of Solids, 53*(7), 1552-1573. [CrossRef]

[12] Pucci, E., & Saccomandi, G. (2002). A note on the Gent model for rubber-like materials. *Rubber chemistry and technology, 75*(5), 839-852. [CrossRef]

[13] Ogden, R. W. (2003). Nonlinear elasticity, anisotropy, material stability and residual stresses in soft tissue. In *Biomechanics of soft tissue in cardiovascular systems* (pp. 65-108). Vienna: Springer Vienna. [CrossRef]

[14] Holzapfel, G. A., Gasser, T. C., & Ogden, R. W. (2000). A new constitutive framework for arterial wall mechanics and a comparative study of material models. *Journal of elasticity and the physical science of solids, 61*(1), 1-48. [CrossRef]

[15] Böl, M., & Reese, S. (2006). Finite element modelling of rubber-like polymers based on chain statistics. *International journal of solids and structures, 43*(1), 2-26. [CrossRef]

[16] Davidson, J. D., & Goulbourne, N. C. (2013). A nonaffine network model for elastomers undergoing finite deformations. *Journal of the Mechanics and Physics of Solids, 61*(8), 1784-1797. [CrossRef]

[17] Cochelin, D. B., Damil, N., & Potier-Ferry, M. (2008). Méthode asymptotique numérique. *European journal of computational mechanics/revue européenne de mécanique numérique, 17*(4), 553-554. [CrossRef]

[18] Cochelin, B., Damil, N., & Potier-Ferry, M. (1994). Asymptotic–numerical methods and Pade approximants for non-linear elastic structures. *International journal for numerical methods in engineering, 37*(7), 1187-1213. [CrossRef]

[19] Vannucci, P., Cochelin, B., Damil, N., & Potier-Ferry, M. (1998). An asymptotic-numerical method to compute bifurcating branches. *International journal for numerical methods in engineering, 41*(8), 1365-1389. [CrossRef]

[20] Hussein, AE, Damil, N., & Potier-Ferry, M. (1998). An asymptotic numerical algorithm for frictionless contact problems. *European Journal of Finite Elements , 7* (1-3), 119-130. [CrossRef]

[21] El Kihal, C., Askour, O., Belaasilia, Y., Hamdaoui, A., Braikat, B., Damil, N., & Potier-Ferry, M. (2022). Asymptotic numerical method for finite plasticity. *Finite Elements in Analysis and Design, 206*, 103759. [CrossRef]

[22] Rammane, M., Mesmoudi, S., Tri, A., Braikat, B., & Damil, N. (2020). Solving the incompressible fluid flows by a high-order mesh-free approach. *International Journal for Numerical Methods in Fluids, 92*(5), 422-435. [CrossRef]

[23] Cadou, J. M., Potier-Ferry, M., Cochelin, B., & Damil, N. (2001). ANM for stationary Navier–Stokes equations and with Petrov–Galerkin formulation. *International Journal for Numerical Methods in Engineering, 50*(4), 825-845. [CrossRef]

[24] Medale, M., & Cochelin, B. (2009). A parallel computer implementation of the asymptotic numerical method to study thermal convection instabilities. *Journal of Computational Physics, 228*(22), 8249-8262. [CrossRef]

[25] Jamal, M., Elasmar, H., Braikat, B., Boutyour, E., Cochelin, B., Damil, N., & Potier-Ferry, M. (2000). Bifurcation indicators. *Acta mechanica, 139*(1), 129-142. [CrossRef]

[26] Rammane, M., Mesmoudi, S., Tri, A., Braikat, B., & Damil, N. (2022). Mesh-free model for Hopf's bifurcation points in incompressible fluid flows problems. *International Journal for Numerical Methods in Fluids, 94*(9), 1566-1581. [CrossRef]

[27] Mezura-Montes, E., & Coello, C. A. C. (2011). Constraint-handling in nature-inspired numerical optimization: past, present and future. *Swarm and Evolutionary Computation, 1*(4), 173-194. [CrossRef]

[28] Pedersen, M. E. H. (2010). Good parameters for particle swarm optimization. *Hvass Lab., Copenhagen, Denmark, Tech. Rep. HL1001*, 1551-3203. [CrossRef]

[29] Wang, D., Tan, D., & Liu, L. (2018). Particle swarm optimization algorithm: an overview. *Soft computing, 22*(2), 387-408. [CrossRef]

[30] MathWorks. (n.d.). particleswarm: Particle swarm optimization. Retrieved from https://www.mathworks.com/help/gads/particleswarm.html

[31] Kuhn, W., & Grün, F. (1942). Beziehungen zwischen elastischen Konstanten und Dehnungsdoppelbrechung hochelastischer Stoffe. *Kolloid-Zeitschrift, 101*(3), 248-271. [CrossRef]

[32] Ouardi, A., Boukamel, A., & Damil, N. (2022).

Towards a macro-chain polymer model using a micromechanical approach. In *Constitutive Models for Rubber XII* (pp. 112-117). CRC Press.

[33] Trinh, D. K. (2011). Méthodes d'homogénéisation d'ordre supérieur pour les matériaux architecturés (Doctoral dissertation, École Nationale Supérieure des Mines de Paris). https://pastel.hal.science/pastel-00677046/

[34] Treloar, L. R. G. (1975). *The physics of rubber elasticity* (3rd ed.). Oxford.

[35] Kennedy, J., & Eberhart, R. (1995). Particle swarm optimization. In *Proceedings of ICNN'95-international conference on neural networks* (Vol. 4, pp. 1942–1948). IEEE. [CrossRef]

[36] Kaliske, M., & Heinrich, G. (1999). An extended tube-model for rubber elasticity: statistical-mechanical theory and finite element implementation. *Rubber Chemistry and Technology, 72*(4), 602-632. [CrossRef]

[37] Marckmann, G., & Verron, E. (2006). Comparison of hyperelastic models for rubber-like materials. *Rubber chemistry and technology, 79*(5), 835-858. [CrossRef]

[38] He, H., Zhang, Q., Zhang, Y., Chen, J., Zhang, L., & Li, F. (2022). A comparative study of 85 hyperelastic constitutive models for both unfilled rubber and highly filled rubber nanocomposite material. *Nano Materials Science, 4*(2), 64-82. [CrossRef]

Ayoub Ouardi received the Ph.D. degree in mechanics and structural computation from Hassan II University of Casablanca, Morocco, in 2025. In parallel with his Ph.D. studies at Hassan II University of Casablanca, he held a doctoral researcher position at Centrale Casablanca. His research interests include hyperelastic constitutive modeling of elastomeric materials, structural analysis, buckling and wrinkling of thin structures, advanced numerical modeling, and nonlinear analysis. (Email: ayoub.ouardi@centrale-casablanca.ma)

Adnane Boukamel received the Ph.D. degree in Solid Mechanics from Aix-Marseille II University, France, in 1988, and the Habilitation to Supervise Research (HDR) in Mechanics from the University of the Mediterranean, Marseille, France, in 2006. His research focused on the mechanical and numerical modeling of elastomeric materials and structures. He has held several academic and leadership positions, including Professor at Centrale Marseille, Director of the Hassan II School of Public Works (EHTP), Scientific Director of the Railenium Institute of Technological Research, Program Director at ECC, and Deputy General Director of ECC in charge of development projects, training, and research activities. He is currently the French Director of École Centrale de Pékin. His research interests include rubber-like material behavior, finite element analysis, multiphysics modeling, and the mechanical and numerical modeling of elastomeric structures. (Email: adnane.boukamel@centralepekin.cn)

Noureddine Damil received the Ph.D. degree in Mechanics from Pierre and Marie Curie University (Paris VI), France, in 1984, and the Doctorate of State degree from Hassan II University of Casablanca, Morocco, in 1990. From 1984 to 2023, he was Professor of Mechanics at Hassan II University of Casablanca, where he held several academic leadership positions, including Vice-Dean of the Faculty of Sciences and Vice-President of the University. He also served as *Maître de Conférences Associé* at the University of Metz (now Université de Lorraine), France, and was invited several times as Visiting Professor. Since 2023, he has been Professor at École Centrale Casablanca and Head of the ISMEC Research and Education Unit. His research interests include computational and structural mechanics, nonlinear analysis, buckling and post-buckling behavior, wrinkling phenomena, structural instabilities, and advanced numerical methods. He has made significant contributions to the development of the Asymptotic Numerical Method (ANM) and its applications to nonlinear mechanical problems. (Email: noureddine.damil@centrale-casablanca.ma)